

**Dissertation**  
submitted to the  
Combined Faculties for the Natural Sciences and for Mathematics  
of the Ruperto-Carola University of Heidelberg, Germany  
for the degree of  
Doctor of Natural Sciences

**Presented by**

**Diplom-Physiker:      Juliane Daartz**  
**Born in:                Rostock**

**Oral examination: May 4th 2011**



# Opportunities and limitations of multileaf collimator based intensity modulated proton therapy

Referees:

Prof. Dr. Uwe Oelfke  
Prof. Dr. Harald Paganetti



## **Abstract**

### **Opportunities and limitations of multileaf collimator based intensity modulated proton therapy**

The vast majority of proton therapy institutes employ passive scattering beamlines. Treatments are delivered by means of laterally and distally conformed homogeneous dose distributions for each beam direction by utilizing spread-out Bragg peaks and custom milled hardware. Most newly built proton facilities rely upon scanned proton beams to provide intensity modulated therapy (IMPT), improvements in treatment planning and delivery workflow. This thesis investigates the benefits of IMPT in fixed proton therapy beamlines and describes aspects of multileaf collimator (MLC) based IMPT delivery. We show that IMPT has the potential to increase the range of applications for fixed proton therapy beamlines. A method for sequencing intensity modulated treatment plans into a set of segments is presented and evaluated based on results obtained for a set of clinical situations. The resulting numbers of segments made delivery technically and logistically feasible. Neutron dose was found acceptable given a well optimized beamline. The dosimetric properties of one specific multileaf collimator were investigated experimentally and compared to custom milled apertures. Small differences were found, but those are clinically insignificant in the vast majority of clinical cases. Finally, an extensive set of measurements for accurate determination of the peak dose as a function of field size is described.



## **Zusammenfassung**

### **Potenzial und Limitierungen von MLC basierter IMPT Anwendung**

Die Mehrheit existierender Protonentherapiezentren nutzt passiv streuende Protonenstrahlanlagen. Patientenbehandlungen basieren auf lateral und distal konformierten homogenen Dosisverteilungen, die von jedem einzelnen Strahl durch spread-out Bragg Peaks und individuell gefertigte Kollimatoren und Kompensatoren geliefert werden. Die Mehrheit der im Bau befindlichen Protonenzentren installiert Scanning Systeme auf Grund ihrer Fähigkeit zu intensitätsmodulierter Protonentherapie (IMPT), sowie ihrer Vorteile im Bezug auf Vereinfachung der Arbeitsabläufe der Bestrahlungsplanung und -lieferung. Das Potenzial von IMPT speziell im Bezug auf fixe Protonenstrahlen liegt in einer Erweiterung derer Anwendungsmöglichkeiten. Diese Arbeit schlägt Multileafkollimatoren (MLCs) für die nachträgliche Ausrüstung existierender passiv streuender Protonenstrahlanlagen zur Anwendung für IMPT vor. Es wird eine Methode zur Sequenzierung von Dosisverteilungen in Serien von Einzelsegmenten vorgestellt und anhand einer Gruppe klinischer Anwendungen evaluiert. Basierend auf der resultierenden Anzahl von Segmenten pro Strahlrichtung wäre die praktische Umsetzung der vorgeschlagenen Methode technisch und logistisch möglich. Die Neutronendosis war akzeptabel mit der Bedingung einer optimal abgestimmten Protonenstrahlanlage. Die dosimetrischen Eigenschaften eines speziellen MLCs wurden untersucht und mit den üblich benutzten individuell gefertigten Messingaperturen verglichen. Die gefunden Unterschiede sind klein und in der Mehrheit klinischer Anwendungen vernachlässigbar. Abschliessend wird die Relation zwischen Strahlmaximumsdosis und Feldgrösse als wichtiger Teil der MLC basierten IMPT Dosislieferung erörtert.



# Preface

This PhD thesis was carried out at the Massachusetts General Hospital (MGH) between November 2006 and December 2010. The work describes benefits of IMPT for fixed passive scattering beamlines and an approach for MLC based IMPT delivery.

The work presented in Chapter 2.1 has in parts been funded by an MGH grant and will be submitted for publication soon. Publications covering the contents of Chapters 3.1 and 3.2 can be found in [1] and [2], respectively. The topic of Chapter 3.2 has been addressed in [3] but has since been much expanded with an improved methodology. Parts of single chapters were presented at international conferences [4] [5] [6] [7]. The contribution for PTCOG 48 in Heidelberg [7] was awarded the PTCOG prize for best Physics poster.



# Contents

<b>1</b>	<b>Introduction to proton therapy</b>	<b>7</b>
1.1	External Beam Radiotherapy . . . . .	7
1.2	Intensity Modulated Radiotherapy . . . . .	9
1.3	Proton Radiotherapy . . . . .	9
1.4	Scope of this work . . . . .	13
<b>2</b>	<b>In Silico Studies</b>	<b>15</b>
2.1	The benefit of IMPT in fixed beamlines . . . . .	17
2.1.1	Introduction . . . . .	17
2.1.2	Methods and Materials . . . . .	18
2.1.3	Results . . . . .	26
2.1.4	Discussion . . . . .	31
2.2	MLC based IMPT - A feasibility study . . . . .	35
2.2.1	Introduction . . . . .	35
2.2.2	Methods and Materials . . . . .	35
2.2.3	Results . . . . .	42
2.2.4	Discussion . . . . .	48
<b>3</b>	<b>Experimental Studies</b>	<b>51</b>
3.1	The dosimetric properties of MLCs in a proton beam . . . . .	51
3.1.1	Introduction . . . . .	51
3.1.2	Methods . . . . .	52
3.1.3	Results . . . . .	56
3.1.4	Discussion . . . . .	62
3.1.5	Conclusion . . . . .	64
3.2	Dosimetry of small Fields . . . . .	65
3.2.1	Introduction . . . . .	65
3.2.2	Methods . . . . .	66
3.2.3	Results . . . . .	69

3.2.4	Discussion . . . . .	75
3.2.5	Conclusion . . . . .	77
<b>4</b>	<b>Conclusions</b>	<b>79</b>
4.1	Summary of Results . . . . .	79
4.2	Limitations of this work . . . . .	80
4.3	Discussion . . . . .	81
4.4	Future Directions . . . . .	83
4.5	Conclusion . . . . .	83
	<b>Bibliography</b>	<b>93</b>





# Chapter 1

## Introduction to proton therapy

### 1.1 External Beam Radiotherapy

Application of radiation in medicine is broadly categorized into diagnostics and therapy. In modern radiotherapy, both are relevant.

The basis of external beam radiotherapy treatment planning are in most cases computed tomography images of the patient acquired in treatment position. A radiation oncologist delineates the target as well as organs at risk on each slice of this image set, and prescribes desired dose levels. Oftentimes additional information from other imaging modalities, such as magnetic resonance and positron emission tomography, is of importance for the definition of visible disease (gross tumor volume, GTV). The majority of indications require expansion of the GTV into a clinical target volume (CTV) to include microscopic disease not visualized on images. To account for uncertainties in positioning of the patient most treatment protocols demand another expansion of the CTV into a planning target volume, PTV [8] [9].

With target and avoidance structures defined, a treatment planner sets up the geometry, for example number of beams and their directions, and dosimetry, for example the weight of each beam, of a treatment plan. Dose is calculated based on electron densities of the tissue as derived from the CT. Treatment is typically delivered by compact medical accelerators using 4 - 25 MV photon beams. Depending on site and clinical indication patients receive doses in a wide variety of fractionation schemes - from more than 20 Gy in a single treatment session up to 80 Gy in small daily fractions of 2 Gy.

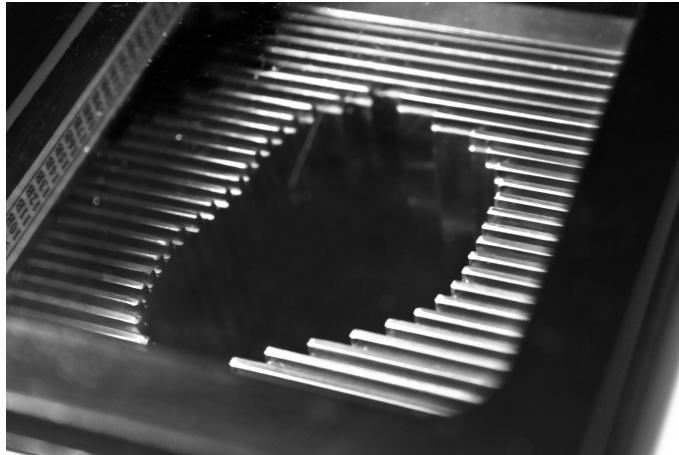


**Figure 1.1:** Front view of the mini-multileaf collimator manufactured by Integra Radionics. Leaves can take individual positions and thus shape arbitrary aperture outlines.

The most common treatment techniques in high energy photon radiotherapy nowadays are 3D conformal (3D CRT) and intensity modulated radiotherapy (IMRT, [10] [11]). In 3D-CRT dose is delivered typically using three to five beam directions. The intensity along the beam's cross section is either constant, or - with aid of additional hardware such as steel or tungsten wedges - sloped in one direction. The beam aperture is modified on a beam-by-beam basis according to the projected shape of the target by custom made blocks or multileaf collimators (MLC, Figure 1.1). The treatment planner chooses wedges, beam shapes and angles in a manual iterative process until the desired dose to target and critical structures is achieved.

The advent of multileaf collimators enabled the routine implementation of more complex intensity modulation than can be provided by wedges. The basic idea of intensity modulated radiotherapy (IMRT) is the two-dimensional modulation of the intensity of a beam across its profile in both directions through the delivery of multiple aperture shapes (segments) per beam (i.e. step and shoot IMRT), or even by continuous variation of leaf positions (dynamic IMRT) [12]. Latest developments in the field include rotational IMRT - continuous variation of leaf positions while rotating the beam around the patient. In the following, we restrict ourselves to an overview of the process for step-and-shoot IMRT delivered with a multileaf collimator.

## 1.2 Intensity Modulated Radiotherapy

The treatment planning process in IMRT is inverted compared to 3D conformal techniques: the user sets constraints for the dose distribution, such as minimum dose to the target and maximum dose for organs at risk (OAR), and starts calculation. During computation each beam is split up into elements, beamlets. The dose contribution of each beamlet to each point in the patient is determined first. The problem of deriving the respective beamlet intensities to achieve a result close to the desired dose distribution in the patient is solved in an automated optimization process. This entire process, however, still requires some manual iteration and an experienced user to obtain satisfactory results. One method of minimizing user intervention is given with multi-criteria optimization [13] [14] (MCO). The treatment planning system calculates a library of treatment plans that all fulfill the desired hard constraints. The user additionally specifies objectives, as for example ‘maximize the mean dose to the target’ and ‘minimize mean dose’ to OAR X, and can navigate between the various plans on the pareto-surface via a graphical user interface.

For the final dose calculation the 2D intensity maps - the outcome of the optimization - still have to be segmented, i.e. translated into deliverable sequences of aperture shapes. Optimal properties for a ‘sequencer’ are to minimize the number of segments and monitor units at the same time.

For an accurate representation of all scatter effects, dose has to be recalculated after segmentation. The resulting dose distribution may be degraded enough to necessitate repetition of the optimization process with altered constraints.

To eliminate this last step, as well as to reduce complexity of intensity maps, and thereby reduction of number of monitor units and segments, direct aperture optimization has been suggested [15] [16] [17]. The reader is referred to Khan [18] for more detail on radiotherapy.

## 1.3 Proton Radiotherapy

While external beam therapy with photons is a widely available treatment technique in thousands of centers worldwide, there are less than 35 operational proton therapy centers. This number is, however, currently experiencing a steep increase. The great promise of

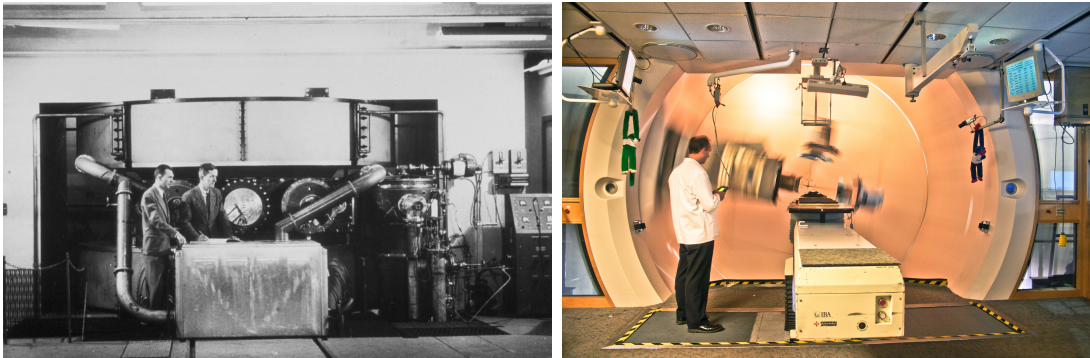


**Figure 1.2:** *Left:* 1949. The first accelerator at the Harvard cyclotron laboratory that was used for patient treatments (From R. Wilson’s library). *Right:* Modern proton gantry (IBA, Belgium) with extended imaging panels for patient setup verification. Currently existing proton therapy facilities feature one particle accelerator, cyclotron or synchrotron, delivering beams to multiple treatment rooms. Total weight of the gantry is approximately 100 metric tons. Facilities have a large footprint in both required space and cost.

proton therapy is the reduction of integral dose compared to photons. The obstacle, on the other hand, is the increased technical challenge and thereby cost.

Photons and protons undergo fundamentally different interaction processes when traversing through media. The depth dose curves for photons is mainly determined by the exponential decrease of primary fluence through Compton and coherent scattering, photo-effect as well as pair production at higher energies. Since photons do not carry electrical charge, they are termed indirectly ionizing radiation - the actual dose is delivered by electrons that were freed by the photons. It takes some distance for longitudinal charged particle equilibrium to be established. This gives rise to a build-up region of the depth dose curve. Protons are directly ionizing. Their main mode of interaction with the medium is collision with electrons, in which the latter are freed from their atoms and receive kinetic energy. Most of those secondary particles have very short ranges, but some receive enough energy to ionize matter themselves (delta rays). Inelastic electromagnetic interactions with nuclei are possible as well, but of minor importance for energies as high as considered here.

The energy loss per unit length due to electromagnetic interactions with electrons in a material has been described for the first time by Bethe and Bloch in their 1930 publication [19]. It was later discussed and modified in various publications [20] [21] [22] [23]. This quantity is called stopping power, and is usually normalized to the density of the considered medium to yield mass stopping power. Stopping power is roughly

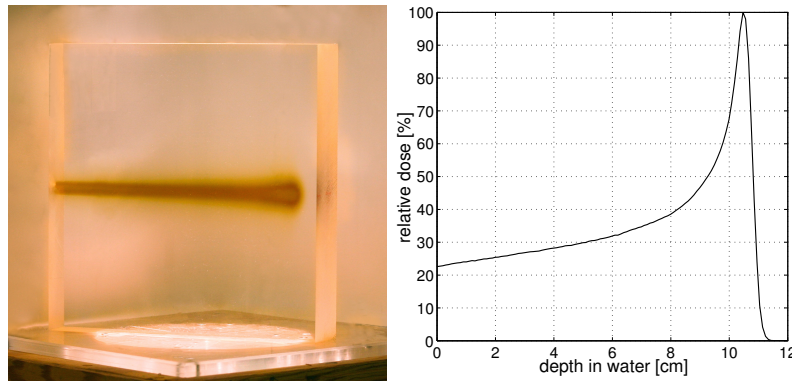


**Figure 1.3:** *Left:* Discoloration of transparent plastic block (dimensions:  $\approx 20 \times 20 \times 5 \text{ cm}^3$ ) by a proton Bragg Peak. Made by Ethan Cascio in a 45 minute irradiation with  $10^{15}$  170 MeV protons, depositing approximately 500 kGy in the entrance region. Finite range and increased scatter in the peak are well visible. Formation of color centers in solid material is a complex process [29]. In the region with the highest dose color actually becomes lighter in our sample. We attribute this to annihilation of color centers due to insufficient heat dissipation because of the high dose rate during irradiation. *Right:* Monte Carlo simulated proton depth dose in water.

proportional to the inverse of the square of the proton's speed. This gives rise to the 'Bragg Peak' (see Figure 1.3), a proton's most valuable property for therapy purposes. The pathlength of a proton in a medium is obtained by integrating the inverse mass stopping power over energy. Since the energy loss per proton electron collision is of statistical nature, the Bragg Peak of a proton beam always has a certain width. This property is called range straggling. In clinical practice a proton beam is usually described by its range, rather than energy. Standard tables are in use for the conversion [20] [21].

The shape of the lateral dose distribution is determined by multiple coulomb scattering (MCS) the elastic electromagnetic interaction of a proton with a nucleus, in which the proton is scattered at an angle. The magnitude of the mean scattering angle is determined by the atomic number of the material, and energy of the proton. A particle therefore never passes through a medium in a straight line, but rather takes a random zigzag course. The mean projected range can be calculated by integrating over the product of inverse mass stopping power and cosine of the average scattering angle. The mean scattering angle was described by Moliere and later approximated by Highland with reasonable accuracy [24] [25] [26] [27]. Safai *et al* [28] have reported on the width of the lateral dose fall-off as a function of depth and energy for collimated and uncollimated proton therapy beams, shown in Figure 1.4.

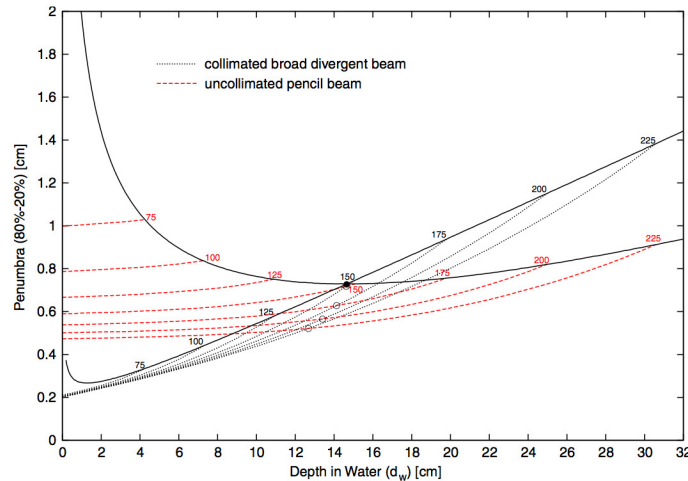


**Figure 1.4:** Lateral penumbra as a function of depth and energy for collimated and uncollimated proton beams. From Safai *et al* [28].

A small fraction of the deposited dose is due to nuclear interactions, in which secondary particles are generated. This latter effect also gives rise to a small buildup of dose in the entrance region to establish longitudinal equilibrium of secondaries created in those nuclear interactions. Some of the secondary particles have long ranges - neutrons are contributing to the dose to the patient distant from the targeted site.

There are two general methods to manipulate proton beams for therapy purposes: passive scattering and beam scanning. The common goal is to deliver the prescription dose uniformly throughout a clinical target, as conformal as possible. Passive scattering, as the name gives away, exploits the scattering properties of protons, see for example [30]. An incoming pencil beam, about 2 cm in diameter, hits a series of scatterers and absorbers in order to shape the lateral and longitudinal form of the dose distribution. A useful diameter of about 25 cm homogenous dose can be produced by a combination of scatterers of various materials and shapes. Spreading of the high dose region in depth is achieved by energy modulation: peaks of several energies are superimposed with appropriate weights to obtain a spread-out Bragg Peak (SOBP). Additional hardware is necessary for lateral and distal conformity, shown in Figure 1.5. These pieces are custom milled for every beam direction used for a patient's treatment. Alternatively to custom milled apertures, multileaf collimators may be employed for 3D-conformal proton therapy [31]. Similar to IMRT it may be possible to use multileaf collimators for intensity modulation in proton therapy.



**Figure 1.5:** In passive scattered proton therapy custom made hardware is necessary for conformation of each treatment field. *Left:* Brass aperture for lateral conformation of the proton beam to the projection of the target. *Right:* Range compensator for distal conformation - each point in the device has a different thickness to adjust penetration depth at each point of the beam's cross section.

Delivery mode number two, beam scanning, makes use of the proton's electrical charge. The basic idea is to sweep a proton beam across the target using magnets. Beam scanning can be subdivided into uniform and pencil beam scanning (PBS). The prior method still uses customized collimators and range compensators to conform the dose since the scanned proton beam is large (several centimeters). At about 1 cm full-width-half-maximum (FWHM) the diameter of the beam for PBS is significantly smaller. In addition to the delivery of uniform dose per field (single field uniform dose, SFUD) without custom hardware, this gives the freedom to perform intensity modulated proton therapy (IMPT) by varying the delivered dose on a point-by-point basis. Beam scanning is technically more challenging, and currently only employed by few proton therapy centers. IMPT is performed by only one center (PSI, Villigen, Switzerland). Various modes of IMPT have been proposed, characterized by the allowed number and positions of beam spots [32]. Lomax concludes that full 3D optimization, i.e. permitting spot positions throughout the entire target, best retains maximum flexibility in designing dose distributions.

## 1.4 Scope of this work

The vast majority of patients treated with proton therapy up to date has received passively scattered proton therapy. Although intensity modulation is inherent to the delivery of a spread-out Bragg peak (SOBP), the dose to the target given per beam is

homogeneous. For true intensity modulated proton therapy this is not the case, target dose is uniform only after the delivery of all beams for a fraction is completed.

In photon therapy intensity modulation is most commonly provided by varying beam shapes with multileaf collimators. Current development in proton therapy makes use of the electrical charge of the particle by sweeping a small beam of 1cm diameter across the target with magnets. Beam scanning enables three-dimensional intensity variation on a point by point basis.

Scanning systems are technically challenging and currently not standard equipment for existing proton therapy facilities, and passive scattering systems will therefore be of use in the near and intermediate future.

We are presenting a feasibility study for the application of multileaf collimators for intensity modulation in passively scattered proton therapy.

Computational studies are reported in chapter 2. Chapter 3 contains experimental investigations.

The following issues are addressed:

- Can IMPT in fixed beamlines offer advantages with respect to conformal (passively scattered) proton therapy? (Section 2.1)
- Is it feasible to deliver IMPT with an MLC, considering treatment time and neutron dose? (Section 2.2)
- What are the properties of a multileaf collimator in a proton beam? (Section 3.1)
- What is the relationship between peak dose per monitor unit (output) and collimator size? (Section 3.2)

# Chapter 2

## In Silico Studies

This chapter contains studies concerning motivation for and feasibility of the use of multileaf collimators for intensity modulation in proton therapy.

In contrast to IMRT, IMPT is not usually associated with multileaf collimators. The ability to sweep protons across a target by magnets makes pencil beam scanning the natural choice for IMPT. Most important benefit of this delivery method is the flexibility to alter beam intensity at any point in the target without the need for custom hardware. The majority of the equipment in the treatment nozzle used for passive scattering is unnecessary for beam scanning. In pencil beam scanning the amount of material within the beam path in the nozzle (and therefore the energy loss) is very small. The neutron dose to the patient is therefore practically reduced to the neutrons created internally in the patient. Custom made hardware for all fields is not strictly required, but has been suggested for minimizing penumbra (for shallow depths with a custom milled collimator [28]) and reducing the number of range layers (using a range compensator).

Much like in IMRT it is possible to employ an MLC for IMPT. This could be done in conjunction with uniform scanning, i.e. delivering homogenous dose per range layer, or passive scattering. The main difficulty for this method is the increased number of monitor units due to the fact that target dose is delivered by multiple small segments for each range layer, with a large fraction of the protons per segment being stopped in the collimator. This translates into increased neutron dose to the patient and increased treatment delivery time. Technically, however, this delivery method is much less challenging to implement than IMPT by means of pencil beam scanning. It does not necessitate alterations of the beamline or treatment nozzle, but only the add-on of the MLC device itself. For passive scattering delivery, an additional benefit is decreased impact of interplay effects for moving targets.

Most of the currently existing facilities operate at least in parts with passive scattering proton therapy. Facilities that are under development or in the planning phase do not exclude passive scattering, so it is likely that this delivery mode will still be in use in the near and intermediate future. In addition, facilities commonly feature one or more fixed passive scattering beamlines. These are especially limited in terms of dose conformity.

Section 2.1 investigates the dosimetric benefits of using IMPT, particularly in the context of fixed horizontal beamlines, and therefore gives motivation for exploring IMPT delivery techniques. Subsequently in section 2.2, where IMPT treatment plans are segmented for application of an MLC, and segmenting results, including neutron dose, are evaluated.



**Figure 2.1:** Patient rotating in the positioner of the fixed horizontal beamline at the Francis H. Burr Proton Therapy Center, Boston, MA. Rigid immobilization of the head as well as additional immobilization of the body is required for rotation of the patient around the cranio-caudal axis. The speed of rotation is about 40 seconds for 90 degrees. The patient is stationary during beam delivery.

## 2.1 The benefit of IMPT in fixed beamlines

### 2.1.1 Introduction

The application of a fixed proton beam has inherent advantages in regards to ease and cost of construction and maintenance compared to a fully rotational gantry, but comes at the potential expense of reduced selection of incident beam angles depending upon the range of motion of the patient positioner. While it has been assumed that maximal freedom in incident beam direction is a necessity for the vast majority of intensity modulated proton therapy (IMPT) treatments, the use of IMPT with restricted beamline angle selection has not been evaluated in detail. The Francis H. Burr Proton Therapy Center (Boston, MA) features a fixed horizontal beamline for intracranial targets, and two fully rotational gantries. For treatment in the fixed beamline patients undergo careful triaging since treatment fields outside the coronal plane involve rotation of the patient around the cranio-caudal axis. This is enabled by the patient positioner [33] but adds strain on the patient and increases treatment time due to the required immobilization (Figure 2.1).

Due to the lack of proximal conformity of the spread-out Bragg peak passive scattering dose distributions are fairly sensitive to incident beam angles. Favorable beam directions usually involve minimum variation of target extension in depth direction, see Figure 2.2. For the majority of cranial patients this results in (at least) a treatment component

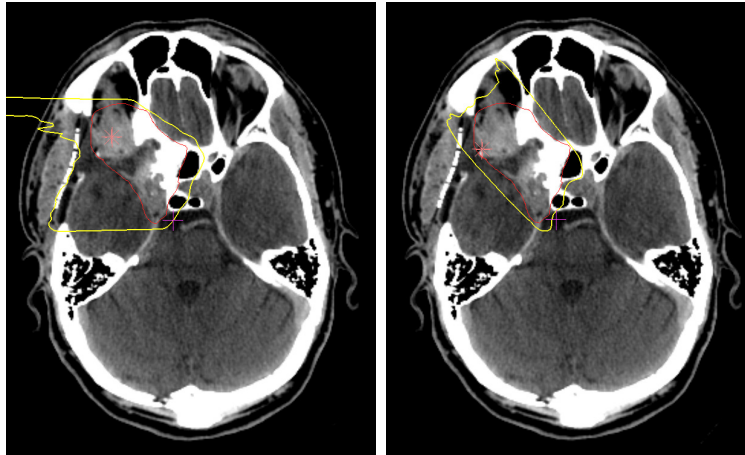


**Figure 2.2:** An example for the quality of proximal conformity with passive scattering for two beam directions. The dose distribution in (a) was calculated with a right lateral field, (b) used a right anterior field. Using the oblique entrance angle improves conformity due to minimum variation of the radiological depth of the target. The yellow line indicates the 90% isodose level, the red line represents the target structure.

outside the coronal plane. In addition, when high doses are delivered to targets in close proximity to critical structures, treatment planning for passive scattering may necessitate patch combinations with two or more fields to create concave dose distributions [34]. In these situations a fully rotational treatment head is beneficial.

In an IMPT treatment plan dose can be flexibly distributed amongst fields and within each beam. The issue of proximal non-conformity does not exist, and shaping of complex dose distributions becomes much easier. We seek to understand whether this flexibility makes IMPT dose distributions less sensitive to the choice of beam angles. Compared to gantries, fixed proton beamlines have the advantage of lower cost and simplicity in regards to construction and maintenance. Our work suggests that the main limitation of fixed beamlines – the restriction of beam angles and therefore compromise of plan quality - may be mitigated by the application of intensity modulated proton therapy.

### 2.1.2 Methods and Materials

This work presents a treatment planning study comparing various plan scenarios for a group of 11 patients.

pat #	Diagnosis	Volume [cc]	Dose [Gy RBE]	Location
		CTV/GTV/boost	CTV/GTV/boost	
1	Low Grade Astrocytoma	64	54.0	Cerebellum
2	Meningioma	27	50.0	Right (Rt) Orbit
3	Acoustic Neuroma	3	54.0	Left (Lt) Cerebello- pontine Angle
4	Meningioma	14	50.0	Lt Anterior Pontine
5	Meningioma	28	50.4	Lt Temporal Lobe
6	Anaplastic Ependymoma	80/32/5	48.6/52.2/57.6	Posterior Fossa
7	Adenoid Cystic Carcinoma	59/4	66.0/76.0	Nasal Cavity
8	Chordoma	26/16	65.0/72.0	Clivus
9	Chordoma	20/13	70.0/77.4	Clivus
10	Meningioma	5	50.4	Rt Cavernous Sinus
11	Chordoma	136/84	70.0/78.0	Clivus

**Table 2.1:** Patient selection diagnosis, target size, prescription dose and target location.

## Patient Selection

This study is limited to intracranial targets only. Patients were chosen as a representative mix of indications typically seen at the Francis H. Burr Proton Therapy center, with regards to size, shape and prescription doses (see Table 2.1 and Figure 2.3). All dose distributions and dose metrics in this work are presented in units of Gy(RBE), i.e. dose in Gray corrected for radiobiological effect [35].

## Treatment Plan Setup

Four treatment plans are compared for each patient: three IMPT plans with varying beam angles and the treated passive scattered (PS) treatment plan as used for actual treatment. Figure 2.4 depicts the allowed beamline configurations for scenarios IMPT A, B and C. All scenarios permit couch rotation in the horizontal plane only. A full example for one patient is explained in Figure 2.5 and Table 2.2.

Plans A utilized a fixed horizontal beamline. In combination with couch rotation this results in beam angles restricted to the coronal plane. Plans B expanded on this by allowing beamline angles in 45 degree increments, and Plans C allowed for a continuous

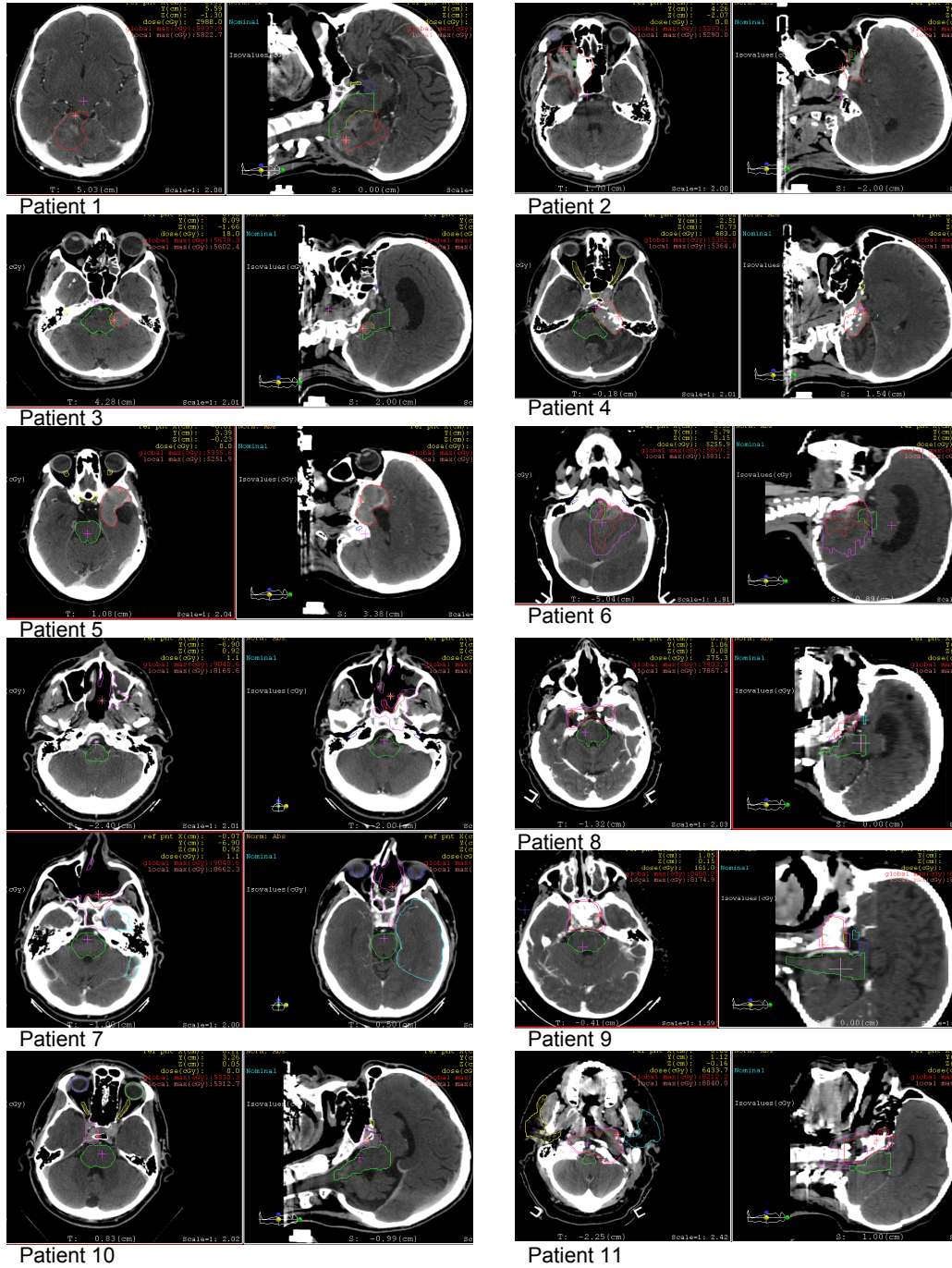
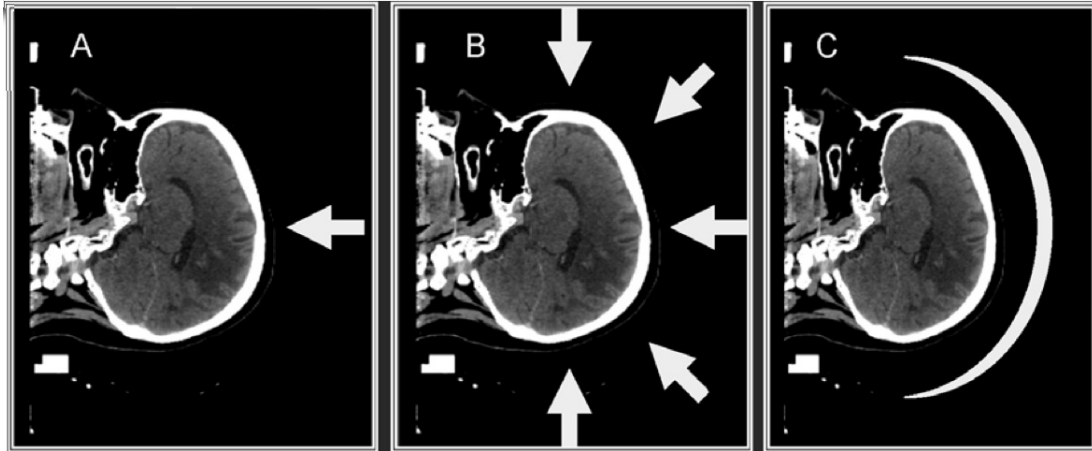


Figure 2.3: The patient selection covered a wide range of target sizes, shapes and locations.



**Figure 2.4:** Allowed beamline configurations for IMPT treatment plans. A: horizontal beamline, B: beam in increments of 45 degrees, C: continuous spectrum of gantry angles. *All scenarios employed a treatment couch for rotating the patient in the horizontal plane.*

spectrum of beamline angles, simulating a fully rotational gantry. Plans C use the same beam directions as the passively scattered treatment plan; though in most cases only a subset of the latter was necessary (for example for patch beam combinations).

beam	plan	gantry angle [deg]	couch angle [deg]
1	A	270	10
	B	315	0
	C	280	0
2	A	270	90
	B	180	0
	C	180	0
3	A	90	-10
	B	135	0
	C	100	0

**Table 2.2:** Gantry and couch angles as used for plans A, B and C for patient 1. The corresponding incident beam directions are visualized in Figure 2.5.

While PS plans were produced using CMS XiO<sup>1</sup> the IMPT calculations were generated using an in-house developed software Astroid [36]. The latter employs multi-criteria optimization, and hence enables the user to choose from a large library of treatment

<sup>1</sup>CMS Inc., St. Louis, MO

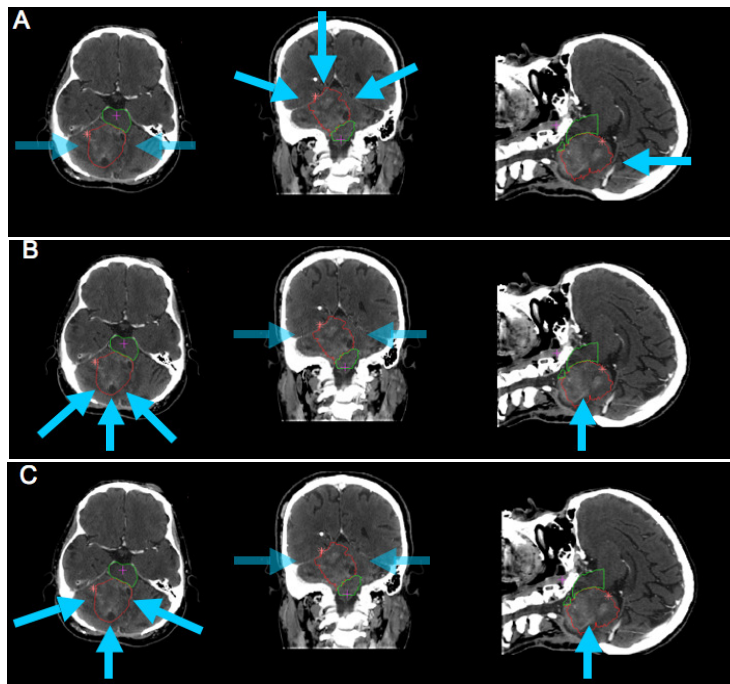


**Figure 2.5:** Visualization of beam angle configurations in axial (*left*), coronal (*center*) and sagittal (*right*) views for patient one to exemplify the treatment plan setup for plan A (*upper*, beam angles only in coronal plane simulating a fixed horizontal beamline), B (*middle*, gantry angles allowed in 45 degree increments) and C (*lower*, free choice of gantry angles). Blue arrows represent incident beams, semi-transparent arrows indicate beam angles not parallel to the plane of the image. Corresponding gantry and couch angles are listed in Table 2.2.

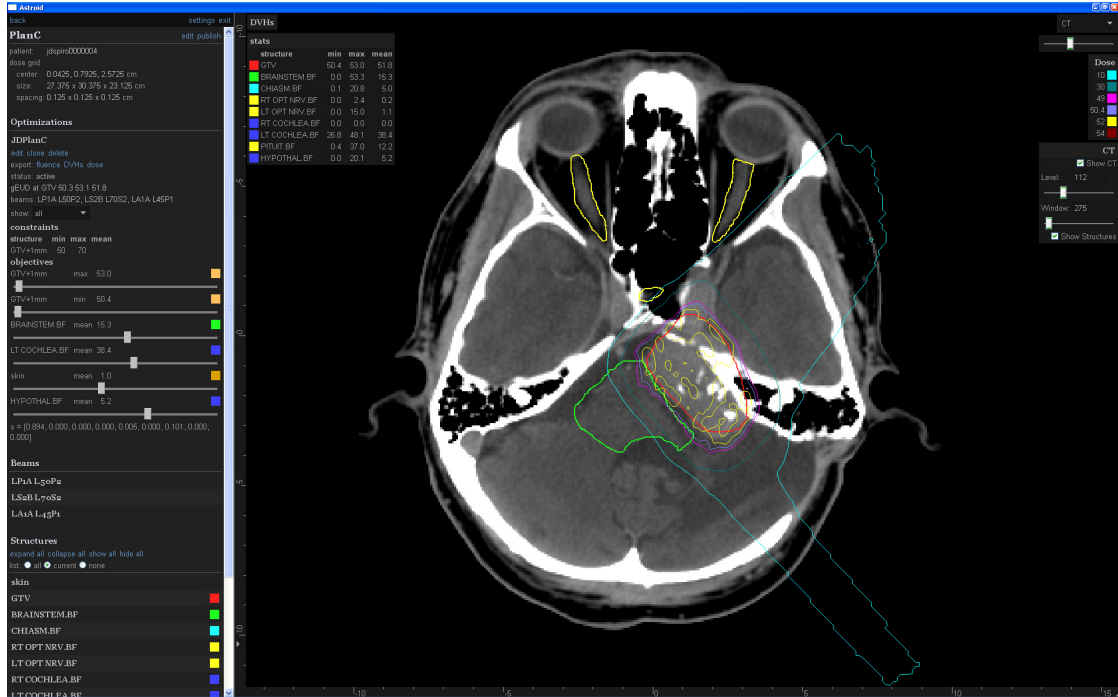


**Figure 2.6:** The treatment planning system Astroid [36]. The panel on the left hand side allows the user to browse through a library of treatment plans by moving sliders.

plans generated to fulfill the given constraints with the specified objectives for target coverage and healthy tissue sparing [37]. Figure 2.6 shows the graphical user interface for Astroid, displaying a treatment plan for patient #4 in this study. The minimum spot size used was 5 mm sigma, defined in air at isocenter for the highest proton energy in the beam data library.

IMPT plans were calculated on the same image data set with 1.25 or 2.5 mm slice thickness, and on the same dose grid ( $1.25 \times 1.25 \times 1.25 \text{ mm}^3$ ) as the clinically used passive scattering plan.

For any plan comparison one has to choose a common denominator. This work utilizes the generalized equivalent uniform dose (gEUD) to the target volume(s) as delivered by the original PS treatment. Thus, the treatment planning goal for IMPT dose distributions was a gEUD that most closely approximated the PS planned value. According to Niemierko [38] gEUD is calculated as:

$$gEUD = \left( \frac{\sum v_i D_i^a}{\sum v_i} \right)^{1/a} \quad (2.1)$$

**Table 2.3:** Parameter **a** used for gEUD calculation

structure	<b>a</b>	structure	<b>a</b>
Brainstem	12	Lacrimal Gland	12
Chiasm	10	Spinal Cord	10
Cochlea	20	Cerebellum	20
Frontal Lobe	10	Parietal Lobe	10
Temporal Lobe	10	Occipital Lobe	10
Lens	6	Parotid Gland	6
Optic Nerve	11	targets	-11
Retina	10		

where  $D_i$  is the dose delivered to the target volume element  $v_i$ , and the parameter **a** describes the volume of interest. Target volumes are assigned a negative **a**, thereby especially penalizing underdosage. Normal tissues have positive **a** parameters to emphasize the high doses. Table 2.3 list values used in this study, as provided by A. Niemierko.

With the constraint of maintaining gEUD to the target, the dose to organs at risk was minimized as much as possible. This is generally a difficult task, since it is impossible to determine whether best possible solution has been achieved. Using MCO, however, enables the treatment planner to easily evaluate a large number of treatment plans that fulfill the general constraints, and therefore increasing the probability of reaching a solution close to optimum. It is important to point out that although the PS dose distribution was used as a baseline for comparison it is not assumed this represented the gold standard of passive scattering treatment plans. Because of the current nature of PS treatment planning – forward, with much time-consuming manual intervention and iteration – the outcome is more subjective and more likely not fully optimized.

## Plan comparison

All evaluated quantities were derived from dose–volume histograms (DVHs). The data analysis consisted of three major points:

a) Quality of the dose distribution within and in proximity of the target. This was assessed by means of conformal index (COIN) and homogeneity index (HI). COIN

evaluates underdosage as well as quality of conformity, it is calculated according to Baltas *et al* [39] as

$$COIN = \frac{V_{GTV.ref}}{V_{GTV}} * \frac{V_{GTV.ref}}{V_{iso.ref}} \quad (2.2)$$

with

$V_{GTV.ref}$ : the volume of the GTV receiving at least the reference dose (in this work the prescription dose is used as reference)

$V_{GTV}$ : the volume of the GTV and

$V_{iso.ref}$ : Total volume receiving the reference dose.

The Homogeneity Index in this work is defined as

$$HI = \frac{D_5 - D_{95}}{D_{mean}} * 100\% \quad (2.3)$$

with  $D_{mean}$  the mean target dose and  $D_5$  and  $D_{95}$  the dose to 5% and 95% of the target volume, respectively.

**b)** Dose to organs at risk whose dose constraints had a direct impact on the quality of the plan. The gEUD was calculated for each OAR and plan setup.

**c)** Dose to healthy brain tissue. The gEUD received by the surrounding healthy brain was calculated for a subset of three patients. Chosen were cases most likely to present a difference between the IMPT treatment plans (i.e. target located inferiorly in the cranium). Brain lobes and cerebellum were delineated on one CT dataset by a neuroanatomist. Deformable registration software (Plastimatch [40]) was used for registering the existing structure set to the remaining two patients.

A data set of this size is difficult to evaluate by plotting DVHs and comparing numbers in large tables across plans and for multiple patients. Therefore all DVH data was summarized into single parameters for each property of the dose distribution (COIN, HI, gEUD). The resulting graphs are no longer patient specific, but rather display results for the entire patient cohort. This was achieved by indexing target volumes, organs at risk and large brain structures, and plotting results versus structure index. Patients had one to three target volumes for a total of 17 targets.

Presented graphs visualize the difference of the evaluated quantities for IMPT plans with respect to the PS value. This, again, does not intend to stylize the latter as the gold standard and best possible passive scattering solution, but rather as a clinically acceptable (and accepted) reference. In addition to the main objective of this work, the inter-comparison of IMPT A, B and C, it also provides a comparison between the two modalities PS and IMPT. Each treatment plan was in addition assessed for clinical acceptability by a radiation oncologist by means of slice-by-slice evaluation of isodose lines.

There is a certain randomness to treatment planning, in that the user specifies objectives and constraints, beam angles, aperture shapes, etc. In short, there are many variables that are manually controlled and it relies upon the planner's judgment to determine when further improvement of a dose distribution is impossible. The data analysis therefore focuses on the composite results for the entire patient cohort, rather than discussing differences on a per patient basis. Specific justification of single data points has been explicitly avoided.

### 2.1.3 Results

#### Dose to targets

Considering all 11 patients the gEUDs to target volumes were within 1% (one standard deviation) of the PS plan. The planning goal – a common gEUD between all plans – is therefore considered fulfilled, and a meaningful comparison of dose distributions can be performed.

The conformal index (COIN), describing dose conformity as well as under-dosage, is depicted in Figure 2.7: Target volumes were sorted by size and the absolute difference in COIN for the IMPT plans with respect to the PS plan plotted. The most striking observation is that all three IMPT plans provide equal coverage and conformity. On average there is a slight improvement of COIN for IMPT versus PS, but the standard deviation is slightly larger than the difference itself.

Conformity of IMPT dose distributions is challenged especially for small targets by non-optimal coincidence of target volume and spot placement grid, because the grid resolution is large compared to target size. Lesions located in low density regions, such as the nasal cavities (patient 7), are affected as well, since radiological distances translate

to large geometrical distances. Therefore conformity for IMPT doses is best with larger volumes and in homogeneous higher density media

The absolute difference in HI in percent of target mean dose for IMPT versus PS is visualized in Figure 2.8. The data show no systematic variation between IMPT plans A, B and C. Averaged over all targets there is no significant difference between IMPT and PS. Inter-patient changes of  $\Delta HI(IMPT - PS)$  are attributed to subjectivity of planning, which we consider, in its effect, analogous to statistical noise. No general trend with target size is visible.

### Dose to organs at risk (OAR)

The OAR were indexed and sorted with respect to patient ID. Figure 2.9 visualizes the absolute differences of gEUD for IMPT and PS dose distributions.

There is an overall improvement in gEUD to the OAR of 4.8 to 5.2 Gy for the IMPT treatment plans as compared to the PS plans, with a fairly large standard deviation of 4.8 to 5.5 Gy. Of importance, the dose to organs at risk did not depend on the incident beam angles for IMPT doses: Plans A, B and C are equivalent in regards to dose to critical structures.

The difference in dose to critical organs between PS and IMPT plans had a large standard deviation. This is mostly due to large reductions achieved for small organs at risk. Reducing dose to small structures was relatively easy in our MCO based IMPT planning software. The MCO software interface utilizes sliders to navigate between treatment plans that fulfill given constraints. The preferred compromise of dose delivered between target and critical structures can often be easily achieved when critical structures have small volumes, resulting in little or no compromise to target dose. The largest reductions in gEUD as depicted in Figure 4 are therefore seen for the smallest structures, such as chiasm and cochlea. Overall, all IMPT plans spared OAR equally well. When evaluating the data in Figure 2.9, it should be emphasized that the data was analyzed as a composite. Differences between IMPT plans A, B and C in single data points are seen but do not represent significant variation for the entire patient cohort. The objective of this study is to identify general trends in the data that are not affected by single outliers and random variations. Given the size of the data set this is a feasible approach.

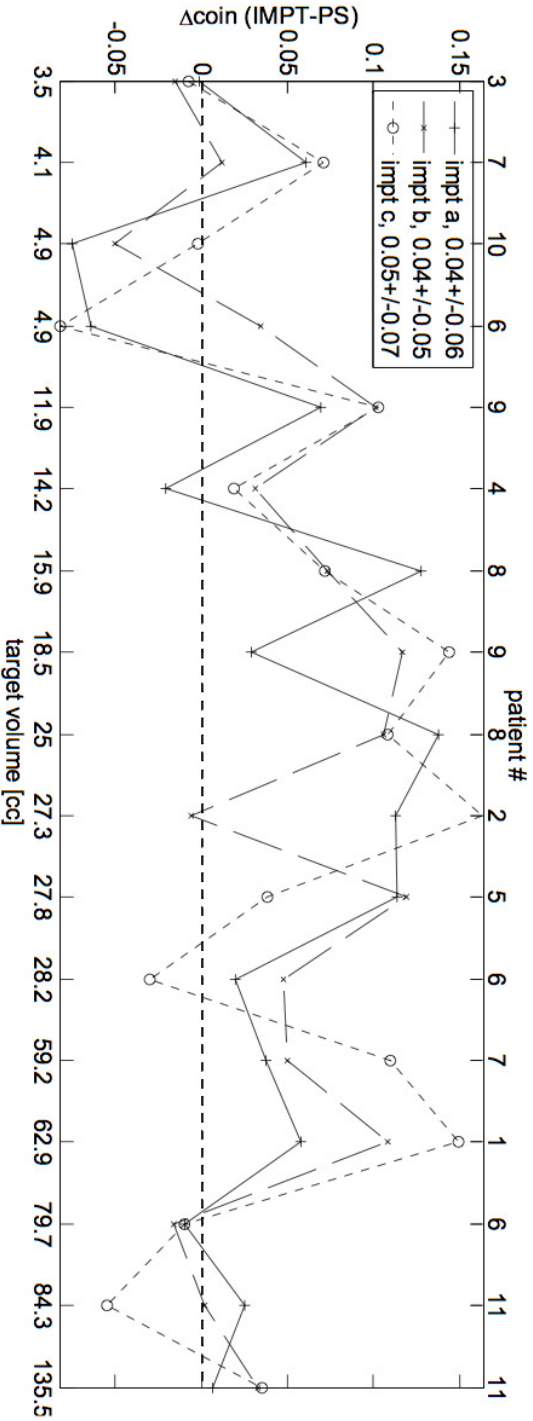


**Figure 2.7:** Conformal Index (COIN). All targets were indexed (1-3 target volumes per patient) and sorted according to volume. The absolute difference in COIN between IMPT and PS plan is plotted. Volumes are labeled with patient ID at the top x-axis. Lines between data points are added purely to guide the eye, not to suggest correlation. There is no significant difference in conformity between the IMPT plans A, B and C.

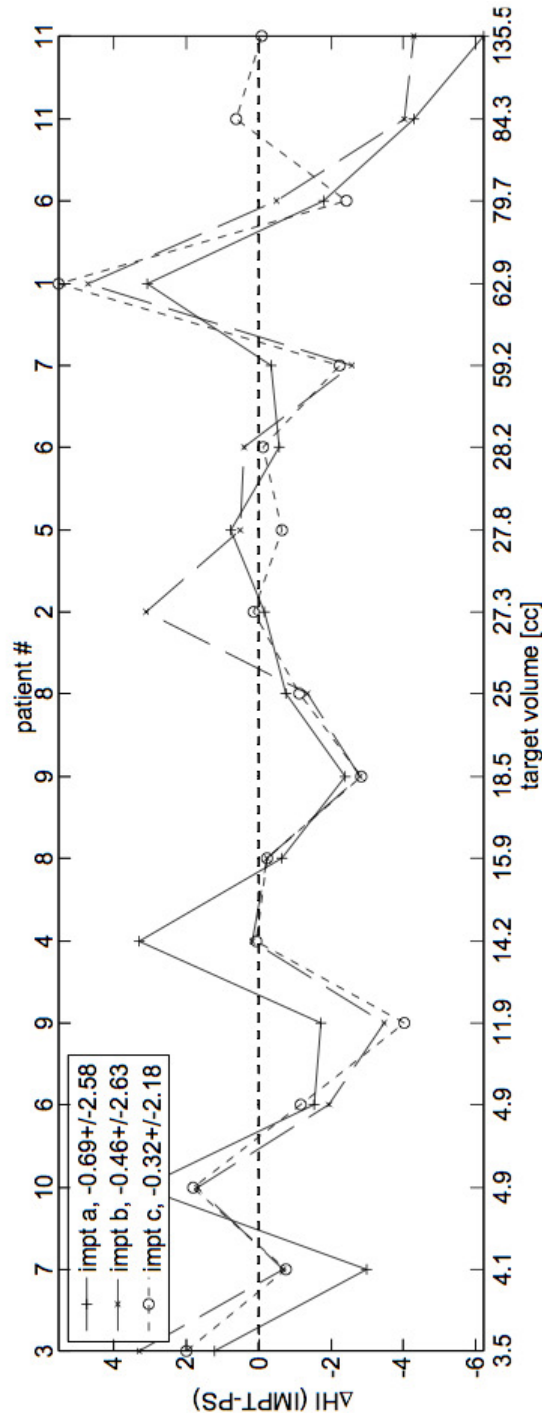


**Figure 2.8:** Difference in Homogeneity Index for each IMPT plan as compared to the respective PS value. Targets are indexed and sorted according to volume size. Patient ID labeled at the top x-axis. Lines between data points were added purely to guide the eye only, not to suggest correlation. Again, no significant difference between IMPT plans A, B and C is observed.

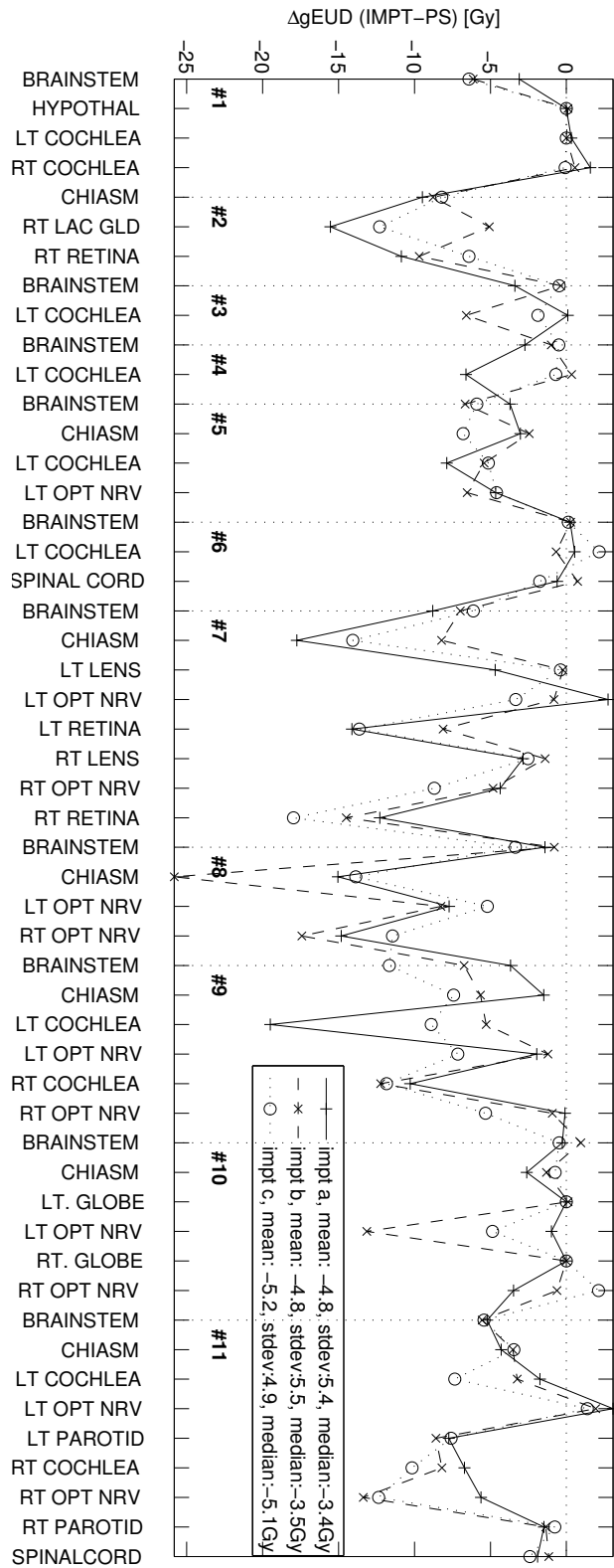


**Figure 2.9:** Absolute differences in gEUD [Gy] to OAR for IMPT A, B and C with respect to PS calculations. All organs are sorted by patient, with vertical dashed lines representing separations between patients. Lines between data points are added purely to guide the eye, not to suggest correlation. On average, there is no difference between IMPT A, B and C.

## Dose to brain lobes

Dose to frontal, temporal, occipital and parietal lobes as well as the cerebellum was assessed for three patients. In Figure 2.10 differences in generalized equivalent uniform doses are plotted versus structure index, sorted by patient ID. The x-axis is labeled with the name of the respective structure. In addition, structures labeled with \* indicate that a target is contained within them, resulting in the gEUD to be dominated by high dose in proximity to the target, rather than by a low dose bath. This also affects structures directly abutting a target (labeled with \*\*). While for one patient there is a significant increase in the gEUD to superior portions of the brain, the other two do not show such general change; dose is rather distributed differently across the brain. Appreciable increase in dose to healthy brain for IMPT plans A is expected for large targets located in the cranial base, which are ideally irradiated with beam directions in the axial plane only, in order to avoid non-target brain tissue (an example is shown in Figure 2.5). This is reflected in the data. For patients # 3 and #11 all treatment plans A, B and C included beam directions in the coronal plane, delivering dose to superior portions of the brain. In these situations IMPT A does not deliver more dose to healthy brain than plans B or C.

### 2.1.4 Discussion

A study assessing the sensitivity of IMPT dose distributions towards the choice of beam angles was presented.

Target gEUD, dose conformity and homogeneity did not differ significantly for the three evaluated IMPT plan scenarios. Dose to organs at risk was slightly decreased for IMPT compared to PS treatment plans, but did not differ amongst IMPT calculations. Larger targets located in the cranial base are treatable with fixed horizontal beamlines, but possibly at the cost of higher dose to healthy brain for a subset of patients.

This limitation of the single fixed horizontal beamline observed for cranial base cases will likely hold true for extra-cranial targets: limiting incident beam directions to the coronal plane will necessitate much larger treatment depths, and will increase the overlap between beams. This is due to the cylindrical shape of the torso. IMPT plans A therefore will likely not be clinically acceptable for the majority of extra-cranial targets. IMPT B however may still provide dose distributions equivalent to what could be achieved with free range of incident beam angles.

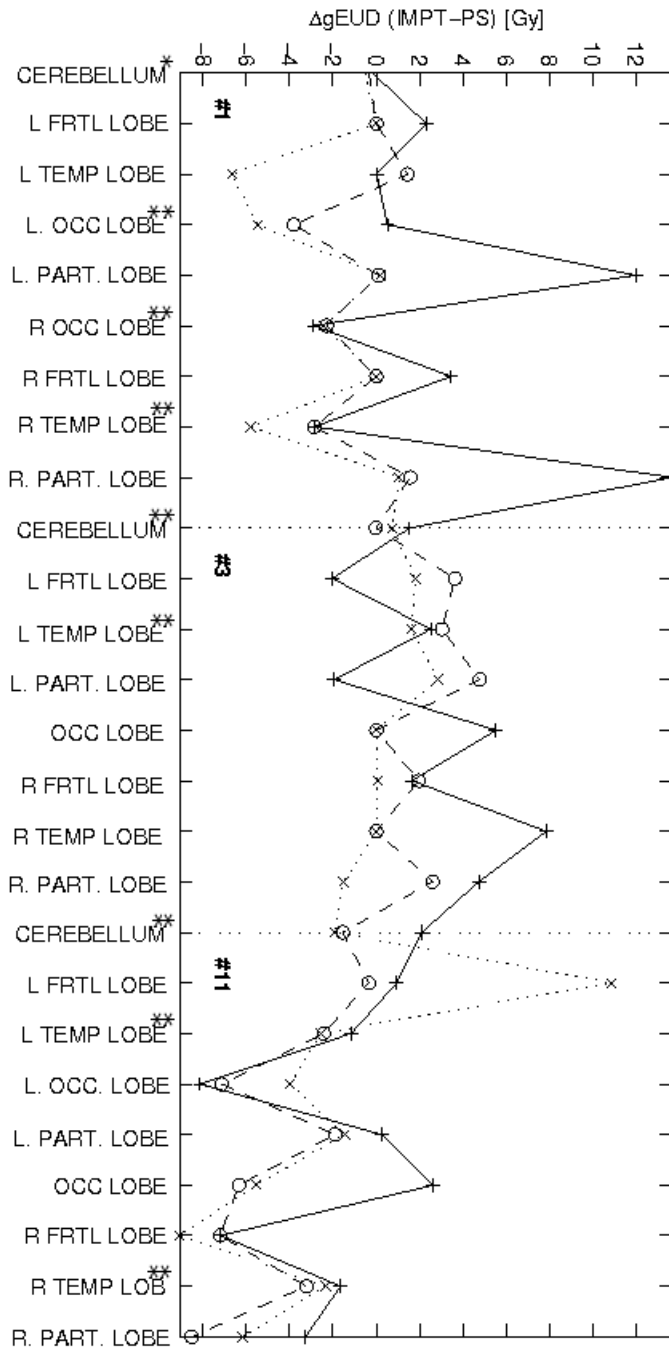


**Figure 2.10:** Absolute differences in gEUD [Gy] to brain lobes and cerebellum for IMPT A, B and C with respect to PS calculations. All organs are sorted by patient, with vertical dashed lines representing separations between patients. Lines between data points are added purely to guide the eye, not to suggest correlation. \* indicates a structure containing a target, \*\* one abutting a target. Dose to certain brain lobes is considerably increased for one patient for IMPT plan A but not so for the remaining two.

The study did not evaluate plan robustness. It has been shown that quality of the nominal plan degrades under robust optimization [41]. It is possible that, once plans are optimized including robustness criteria, a difference between IMPT A, B and C may be found. Dose calculation uncertainty is specific to treatment depth and degree of inhomogeneity traversed by the beam. This could potentially be increased for plans A since the available beam directions might not allow avoidance of inhomogeneities. Furthermore IMPT A plans may require larger ranges. This will increase the absolute range uncertainty as this is a consequence of HU to stopping power conversion and general HU uncertainties. These are in clinical practice considered to be proportional to radiological depth. Similarly, the small dosimetric differences noted for the IMPT versus PS treatment plans may change in the face of uncertainties.

The literature suggests that larger improvements can be noted for IMPT versus PS when using smaller spot sizes [42] [43]. This is due to the availability of steeper dose gradients and therefore better dose conformity. Steep gradients on the other hand negatively influence plan robustness [41].

Although there is no published study dedicated to a comparison of passive scattering and IMPT, MacDonald *et al* [44] [42] concluded there may be improvements of dose to OAR for IMPT in a comparison of three patient treatment plans. Multiple studies performed at the Paul Scherrer Institute (Switzerland) compared PBS single-field uniform dose (SFUD) with passively scattered SFUD dose distributions [45] [46], and later PBS SFUD to IMPT [47] treatment plans. In those three publications, no significant differences between PS and PBS SFUD doses were noted, while IMPT improved OAR sparing compared to PBS SFUD.

A more thorough investigation than the one presented here may be feasible with a beam angle optimization [48] [49] framework that incorporates fluence optimization into the process. This may enable fast evaluation and comparison of a large number of dose distributions obtained with various sets of beam angles.

## Conclusion

IMPT dose distributions in this study were not sensitive to the choice of beam directions when evaluating dose to the target and organs at risk. The patient sample included a large spectrum of intracranial indications in terms of target size, location and prescription dose. This gives good indications that it will be useful to add the capability for application of

intensity modulation to facilities with existing fixed passive scattering beamlines. IMPT overcomes the dosimetric limitations that exist for passive scattering in situations with limited beam angles and will therefore increase the spectrum of indications treatable in a fixed beamline.

## 2.2 MLC based IMPT - A feasibility study

### 2.2.1 Introduction

The previous chapter illuminated the benefits of intensity modulated proton therapy especially in fixed proton beamlines. There are two approaches to actually implement IMPT - by means of scanned pencil beams or, as common in photon therapy, using a multileaf collimator. The advantages of the latter are that it is a proven technology (for photon therapy) and the absence of a need for modifications of the proton beamline itself. The multileaf collimator can be implemented as an add-on module. This is especially useful for retro-fitting existing passive-scattering proton beamlines for IMPT applications.

In the following, an approach to calculate and evaluate intensity modulated proton beam plans for the delivery with a multileaf collimator (MLC) is presented.

In photon intensity modulated therapy beam-on time is increased compared to 3D-conformal therapy since the dose for a beam is now delivered by a sequence of small subfields, together constituting a 2-dimensional intensity map. In proton intensity modulation there is one such two-dimensional intensity map per range layer. This may increase the beam-on-time even more. Not only is this an issue of efficiency and treatment time, but also of secondary dose to the patient. As discussed in the introduction, Chapter 1, protons undergo nuclear interactions when traversing through media. Neutron dose has been the subject of constant debate in proton therapy, especially in the recent years [50] [51]. A possible increase in neutron dose is an undesired side effect if intensity-modulated proton therapy is applied with a multileaf collimator. A separate section was therefore dedicated to the detailed discussion of this aspect.

### 2.2.2 Methods and Materials

#### Patient Selection

This study is restricted to lesions located in the cranium, because those are the cases treated in our fixed beamline in which we are considering to apply a multileaf collimator.

The patient cohort is comprised of six cases, with diversity in intra-cranial target locations, sizes and prescription doses (see Table 2.4).

pat #	Volume [cc]	Dose [Gy RBE]	Location
	CTV/GTV	CTV/GTV	
1	27	50.0	Rt Orbit
2	14	50.0	Lt Anterior Pontine
3	28	50.4	Lt Temporal Lobe
4	19/12	58/68.0	Clivus
5	24/9	54.0/58.0	Base of Skull
6	123/78	72/78	Clivus

**Table 2.4:** Patient selection - target size, prescription dose and target location.

## Planning Techniques

For a detailed description of the treatment planning system employed for this work, Konrad, the reader is referred to Nill [52]. Treatment planning in Konrad begins with setting up isocenter, beam directions and dose constraints for targets and organs at risk.

The cross section of a proton beam is divided into beamlets whose positions in beam's eye view are spaced according to a grid with a resolution set by the user and defined in the isocenter plane. For proton therapy there is one such grid per energy used in the treatment plan. One pencil beam is sent through each grid point, and dose contributions from all beamlets  $i$  to all points  $j$  are calculated and stored in a matrix  $D_{ij}$ , the dose influence matrix.

This calculation is based on a library of pristine Bragg peaks generated by Monte Carlo simulation, see Figure 2.11 [53]. The dose distribution of a pristine peak is determined by the beam's energy and angular distributions. Both depend on machine characteristics as well as the properties of the traversed medium. In practice, the data library contains - as a function of depth - both angular sigma and the dose deposited for each pristine peak. A beam data library is commonly described by the sigma *in air* of the angular spread for the deepest peak in the data set. This is the minimum beam width for the ensemble, since higher energy protons are less affected by scatter in air prior to incidence on the patient. The library of pristine Bragg peaks used for this publication had a minimum beam sigma of 5 mm, and contained peaks with ranges in 5 mm increments.

Utilizing  $D_{ij}$  the optimizer iterates the weights of all beamlets  $i$  until an objective function, describing the difference between current and desired dose distribution, is minimized. At the end of the optimization the dose distribution for a beam is characterized

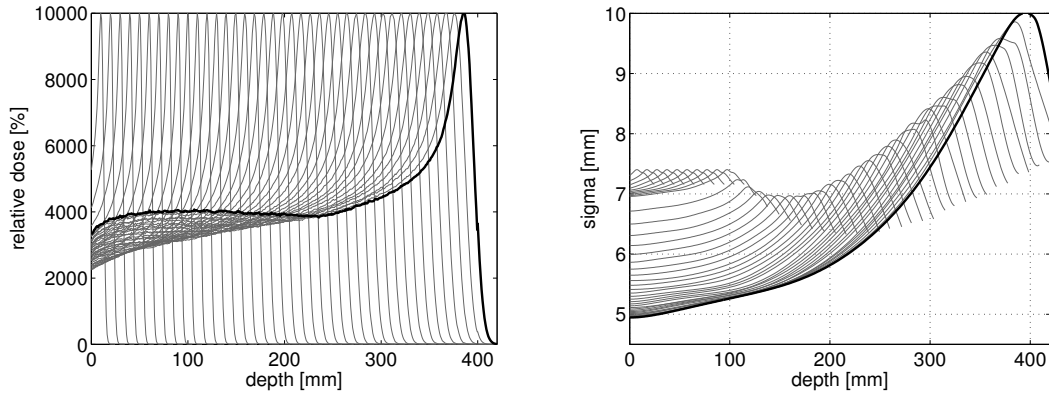


**Figure 2.11:** The Konrad beam data library. For clarity of the graph only every other peak is displayed. *Left:* Depth dose curves. The dose at each depth represents the integral dose in the plane at that depth. All curves are normalized to a weight at peak depth of 10000. In a gaussian distribution the maximum peak height equals the integral divided by a factor  $\sigma\sqrt{2\pi}$  *Right:* Angular sigma of the pencil beams as a function of depth.

by  $i$  beam spots with a certain energy, beam weight and position ( $x$  and  $y$  in beam's eye view coordinate frame). In Konrad these parameters are stored in "steering" (energy and spot position) and "beam weight" (spot weight and position) files.

Figure 2.11 shows that at depths of interest up to 20 cm the beam sigma in our data set is about 7 mm. According to Bortfeld *et al* [54] the optimal sampling resolution is about one sigma of the considered pencil. We chose a spot grid resolution of 10 mm with the aim to simplify the resulting intensity maps. The impact of compromising the sampling distance to this extent, however, is not expected to have an appreciable influence on the dose distribution, given the fact that intensities are optimized over multiple beams at the same time. In order to validate that this does not compromise the dose distribution treatment plans were optimized with both 7 and 10 mm spot grid resolution.

It is important to note that this study does not address the deliverability with any one specific multileaf collimator. Certainly the physical properties, such as leaf width or leaf end shape, have a significant impact on the dose distribution. This work, however, provides an initial feasibility study to assess whether the delivery of intensity modulated dose distributions can be quantized in a way that permits the use of a multileaf collimator.

As mentioned above the optimizer can utilize pristine peaks from a library with 5 mm spacing in depth. This results in a large number of range layers in the target. Aiming to reduce the number of layers utilized for the calculation a third optimization was

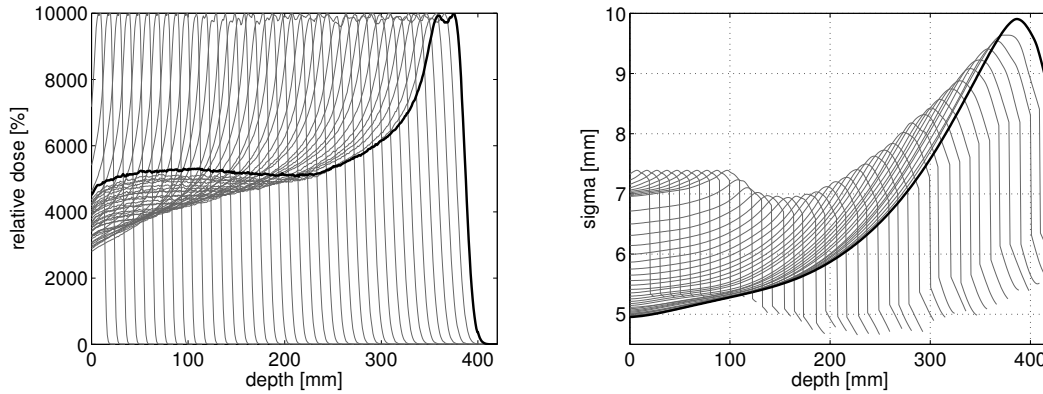


**Figure 2.12:** The modified Konrad beam data library. Displayed is every other peak for clarity. *Left:* The optimization is now based on a series of 2-peak SOBPs. *Right:* Sigmas for the new peaks were approximated by the weighted average of the two sigmas at each depth. The weights of the peaks were obtained through an optimization of depth dose homogeneity in the peak region.

performed on the basis of a data library based on small, two-peak SOBPs rather than pristine peaks. Since now one range layer can provide dose coverage over a larger extent in depth than was possible with a narrow pristine peak fewer range layers are needed to produce dose distributions in accordance with the given constraints. To force Konrad to use only every other peak from the beam data library it was necessary to use the steering files obtained during the previous optimization (10 mm grid resolution, single pristine peak data library), eliminate spots of every other energy, and optimize based on these sparse steering files. The purpose of this third optimization is to investigate whether a reduced number of range layers results in reduced number of segments while maintaining equal plan quality as for the original number of range layers.

In order to sequence the intensity distribution for a beam for the delivery with a multileaf collimator the beamlet intensities were first sorted according to energy and then arranged in a matrix according to their position in the beam's eye view coordinate frame. The result was one intensity map per range layer.

During optimization in Konrad there are no constraints on the complexity of the intensity distribution. The only limits are the spot positions and the quality of the beam data library. To reduce the complexity of intensity maps produced during the optimization process, however, the intensity maps are pre-processed prior to segmentation. The aim is, again, to sequence intensity distributions with as small a number of segments as possible. The less modulated an intensity map, the fewer segments are needed.

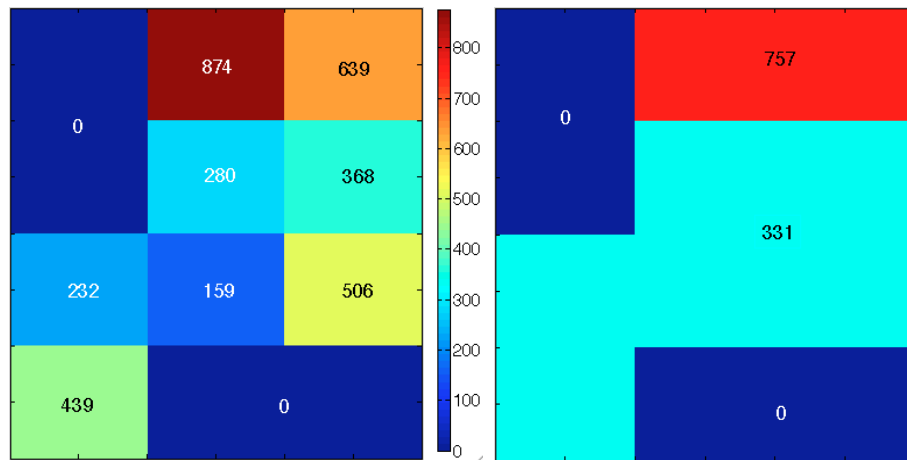


**Figure 2.13:** An example for simplification of an intensity layer. *Left:* Original intensity map for one layer (arbitrary units). *Right:* Simplified map after pre-processing. Allowed were only two intensity levels for this layer. During the calculation these two are first set to the minimum non-zero and the maximum value of the original map (here: 159 and 874). Then all values are grouped with respect to the one discrete intensity level they match most closely (group 1: 874 and 639; group 2: 280, 368, 232, 159, 506 and 439). Their beam weight was subsequently set to the group average (757 and 331), and finally the segments assigned their respective, new values. This map is now deliverable in two segments.

Pre-processing was performed on a beam-by-beam basis. Each range layer was assigned an importance based on its absolute dose contribution and dose variation within the layer. Limiting the total number of intensity levels over the three-dimensional intensity cube, the number of intensity levels per range layer was proportional to the importance of this layer. In this step, at least one intensity was permitted per layer, no layer was omitted.

Within a range layer, the intensity levels were first distributed at equal increments between and including the minimum non-zero and maximum beamlet weight (with zero as an additional allowed value). Next, beamlets were grouped with respect to the one discrete intensity level they match most closely. Their beam weight was subsequently set to the group average, resulting in non-uniform spacing between intensity levels. This is demonstrated with a simple example in Figure 2.13.

Figure 2.14 shows the graphical user interface programmed in MATLAB<sup>2</sup> for the purpose of segmenting intensity maps that were calculated from Konrad optimization output data (beam weight, spot position and energy) and beam data. The GUI was used

<sup>2</sup>The MathWorks Inc., Natick, MA

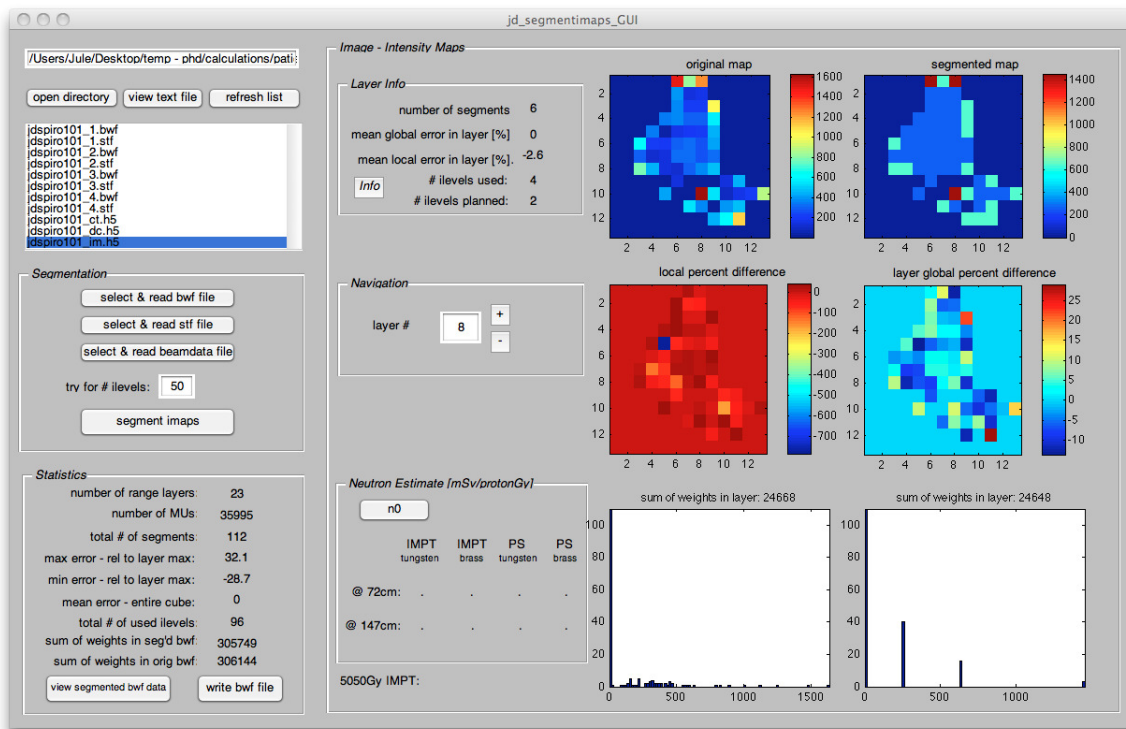


**Figure 2.14:** Matlab GUI for segmentation of intensity maps created from Konrad beam weight files, steering files and beam data library. Neutron dose is estimated for passive scattering and MLC based IMPT delivery.

to steer and evaluate segmentation results, such as global and layer specific statistics for a beam, as well as calculation of an estimate for neutron dose.

The preprocessed maps were then sequenced using the algorithm by Engel [55], as implemented by Kofi Deh. The required number of segments is reported. Those segmented intensity maps were read back into Konrad, so that the final step in the planning process was dose calculation based on the newly determined intensity distribution.

This procedure was an iterative one - the beams were re-segmented until the desired compromise between plan quality and number of segments was achieved. For this purpose doses were compared with an approach similar to the method used in chapter 2.1. Targets were indexed and gEUDs for targets and OAR as well as homogeneity index for targets plotted. A segmented dose distribution was considered acceptable if target gEUD agreed within 2.5% and HI within 5% of the original plan.

In summary, five dose distributions were calculated: Optimization **I** was performed with a 7 mm spot grid resolution. For later segmentation plans **II** were optimized with a resolution of 10 mm. For plan **III** we modified the beam data library and optimized

plan #	I	II	III	IIs	IIIs
spot grid resolution	7 mm	10 mm	10 mm	II segmented	III segmented
beam data library	1pp	1pp	2pp		

**Table 2.5:** Overview of calculated treatment plans. Numbers I – III are plans as optimized by Konrad. Dose distributions for IIs and IIIs represent the resulting dose distributions after segmentation of the Konrad optimized intensity distributions. 1pp and 2pp denote single pristine peaks and 2-peak SOBP Konrad beam data libraries, respectively.

using mini-SOBPs and a grid of 10mm. Finally, plans II and III were sequenced and dose re-calculated with the new, segmented intensity distributions, resulting in plans **IIs** and **IIIs**. An overview of the various plans is given in Table 2.5.

## Neutron Dose Estimate

Neutrons are an unwanted byproduct in proton therapy. There are three main sources of neutrons: the beam modifying devices in the treatment nozzle, the beam limiting device (aperture), and the patient. For our fixed beamline the contribution from the aperture is the largest, and increases with smaller aperture size and higher beam energy. Using a multileaf collimator for intensity modulation requires delivery of an increased number of monitor units and smaller fields, with both factors increasing the neutron dose to the patient.

We estimated the neutron dose resulting from a delivery of the calculated IMPT dose distributions with a multileaf collimator. The neutron dose data as presented in section 3.1 served as a basis for calculating the estimate. In brief, neutron dose was measured with Bonner spheres at multiple positions lateral of the central beam axis for various proton energies and multileaf collimator openings. A quality factor of 5.9 was used for the conversion to dose equivalent. Neutron dose for a given MLC segment was then estimated by interpolating the data set given proton energy and are of the segment. The reader is referred to section 3.1 for a detailed description on the measurements.

Using this dataset allowed us to accumulate the neutron dose contribution on a segment-by-segment basis. Neutron dose to the patient strongly depends on the distance from the collimator. Values given here represent the neutron dose at a distance of  $\approx 75$

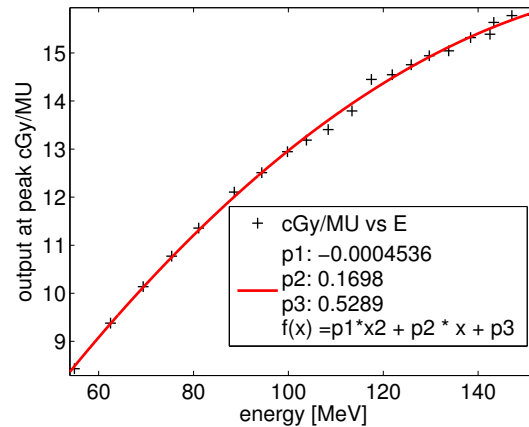


**Figure 2.15:** Absolute dose calibration of monoenergetic Bragg peaks for a 50 mm field radius for the fixed horizontal beamline at the F.H.B proton therapy center.

cm off isocenter, perpendicular to the beam direction, a position relevant for the most sensitive patient group, pregnant women. Neutron dose in forward direction is larger than in lateral direction by a factor of  $\approx 1.1 - 3$  depending on proton energy and air gap.

**IMPT.** The energy and area of each segment was used for two-dimensional interpolation of the data set given in Figures 3.7 and 3.8 to obtain the neutron dose per proton Gray segment by segment. The total neutron dose given by any single beam is calculated by summation of all segments' contributions.

**Passive Scattering.** The IMPT neutron doses are contrasted to a similar estimate for a passive scattering delivery. The minimum and maximum range needed for a beam in the IMPT plan were used to estimate range and modulation needed to deliver a homogeneous dose to the target via an SOBP. The number of pristine peaks constituting this SOBP, their energies and number of monitor units were determined using LAMINATE [56]. The dose per monitor unit at peak depth for monoenergetic beams was calculated from a fit to measured data, see Figure 2.15. The field size was approximated by the largest extent of a beam over all depths.

## 2.2.3 Results

### Evaluation of dose distributions

To illustrate the degradation of dose distributions after segmentation, target dose volume histograms for patient #1 and various segmentations of plan II are displayed in Figure

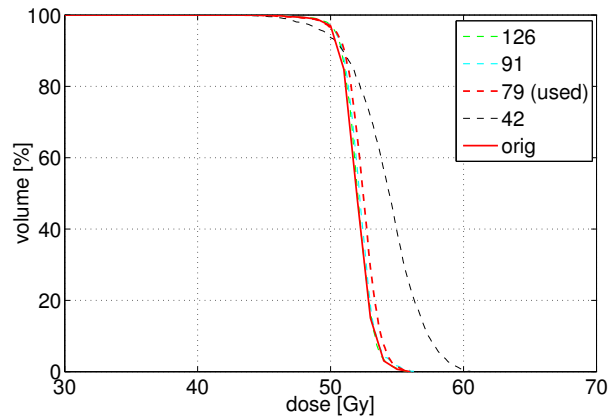


**Figure 2.16:** Target DVH for patient # 1 as a function of the average number of segments per beam. The DVH for the original non-segmented dose distribution is plotted in solid red. Three beam directions were used for this treatment plan.

2.16. There were three beam directions in this plan. The legend indicates the average number of segments per beam. A too large reduction in the number of segments leads to severe degradation of the treatment plan. When utilizing a large number of segments, the original dose distribution is reproduced, as is the case in Figure 2.16 for the average of 126 segments per beam. Reducing this by  $\approx 30$  segments per beam caused a minor degradation of the DVH for this plan. Sequencing with 79 segments per beam yielded the best compromise between plan quality and segment number in agreement with the constraints for gEUD and HI. Limiting the amount of segments even more degraded the dose distribution to an unacceptable level.

Figures 2.17 and 2.18 show the quality of the resulting dose distribution using optimization I (7 mm spot grid, original beam data library) as a reference. Target gEUDs of all plans agree within 2.5% maximum deviation. The mean difference in gEUD with respect to plan I was 0.03%, 0.06%, 1.03% and 0.78% for plans II, III, IIs and IIIs, respectively. The homogeneity index, i.e. the width of the fall-off of the dose volume histogram between the 5% and 95% dose levels of the target dose, proved to be the more sensitive parameter. The average absolute difference in HI compared to plans I was 0.73%, 2.19%, 1.59% and 3.04% for plans II, III, IIs and IIIs, respectively. That means our segmentation of optimized plans caused  $\approx 1\%$  increase of the homogeneity index. There were no significant differences with regard to dose to OAR. The differences in the mean gEUD of the OAR between the plans were small compared to the standard deviation.

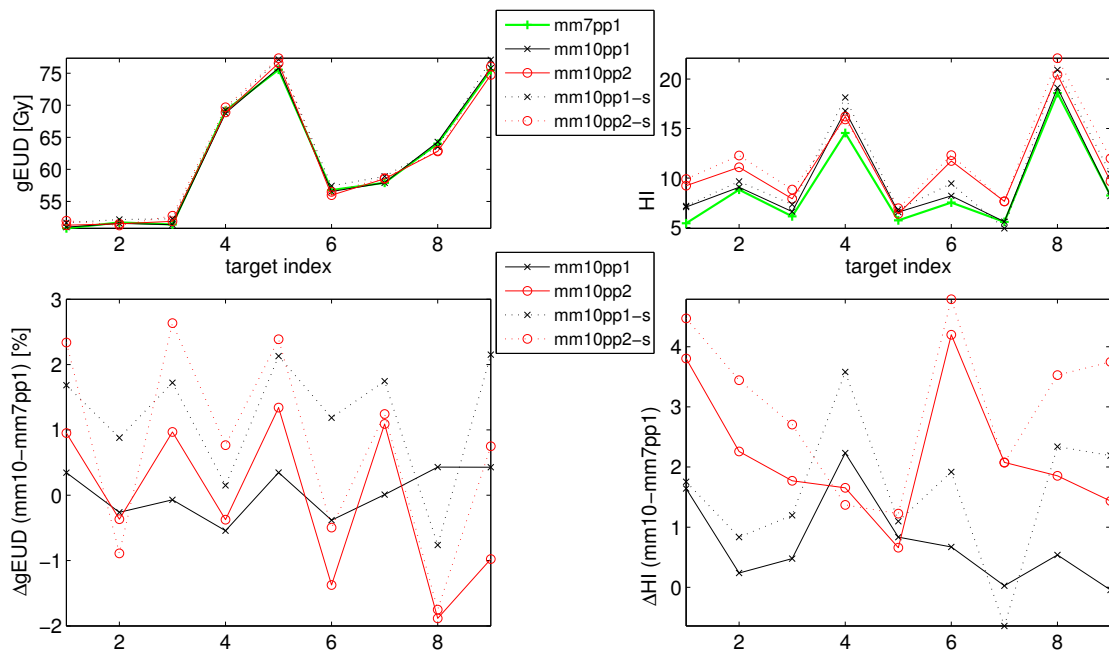


**Figure 2.17:** *Left Upper:* absolute generalized equivalent uniform dose (gEUD) for all target volumes and plans versus target index. *Left Lower:* Differences in target gEUD of all plans with respect to plan I. *Right Upper:* Homogeneity index (HI) for all target volumes and plans versus target index. *Right Lower:* Differences in HI of all plans with respect to plan I. Data points have been connected to guide the eye.

It was possible to produce plans within the defined acceptance criteria of  $\pm 2.5\%$  target gEUD and  $\pm 5\%$  homogeneity index. How closely the segmented dose distributions resemble the original optimizations depends strongly on the number of segments allowed, see Figure 2.16.

### Segmentation results

The average number of segments per beam for all patients is depicted in the left upper panel of Figure 2.19. This number averaged to 73 and 40 for plans IIs and IIIs, respectively. Per layer these numbers translate into 4.9 and 5.6 (Figure 2.19, left middle panel). In total, over all beams, the average number of range layers was 49.3 and 23.7, respectively (Figure 2.19, left lower panel).

### Neutron dose estimate

The correlation of the relationship of neutron dose versus number of segments is illustrated in Figure 2.20, as calculated for patient # 1 plan IIs. The curve levels off at  $\approx 80$  segments per beam. This is a consequence of limiting the numbers of segments via a restriction of the number of intensity levels. With only few intensity levels allowed there will be some very large segments in a beam, but most of the dose is delivered by many small segments that have a much larger contribution to neutron dose. With more intensity levels allowed the histogram of total dose delivered by a field size in a beam shifts towards the medium segment sizes, with fewer very small segments, and very few, if any, very large segments. That means that per segment less neutron dose is delivered. This effect of field size counteracts a continuous increase in neutron dose due to increased number of segments.

Per delivered proton Gray the neutron dose for the passive scattered plan and plans IIs and IIIs was on average 0.1 mSv/Gy, 0.8 mSv/Gy and 0.6 mSv/Gy, respectively, as shown in Figure 2.19, right middle panel. This corresponds to an average increase in neutron dose for MLC based IMPT delivery by a factor of 6 - 8 (Figure 2.19, right lower panel). For completeness, the total neutron doses over the entire treatment course are plotted in the right upper panel of Figure 2.19.

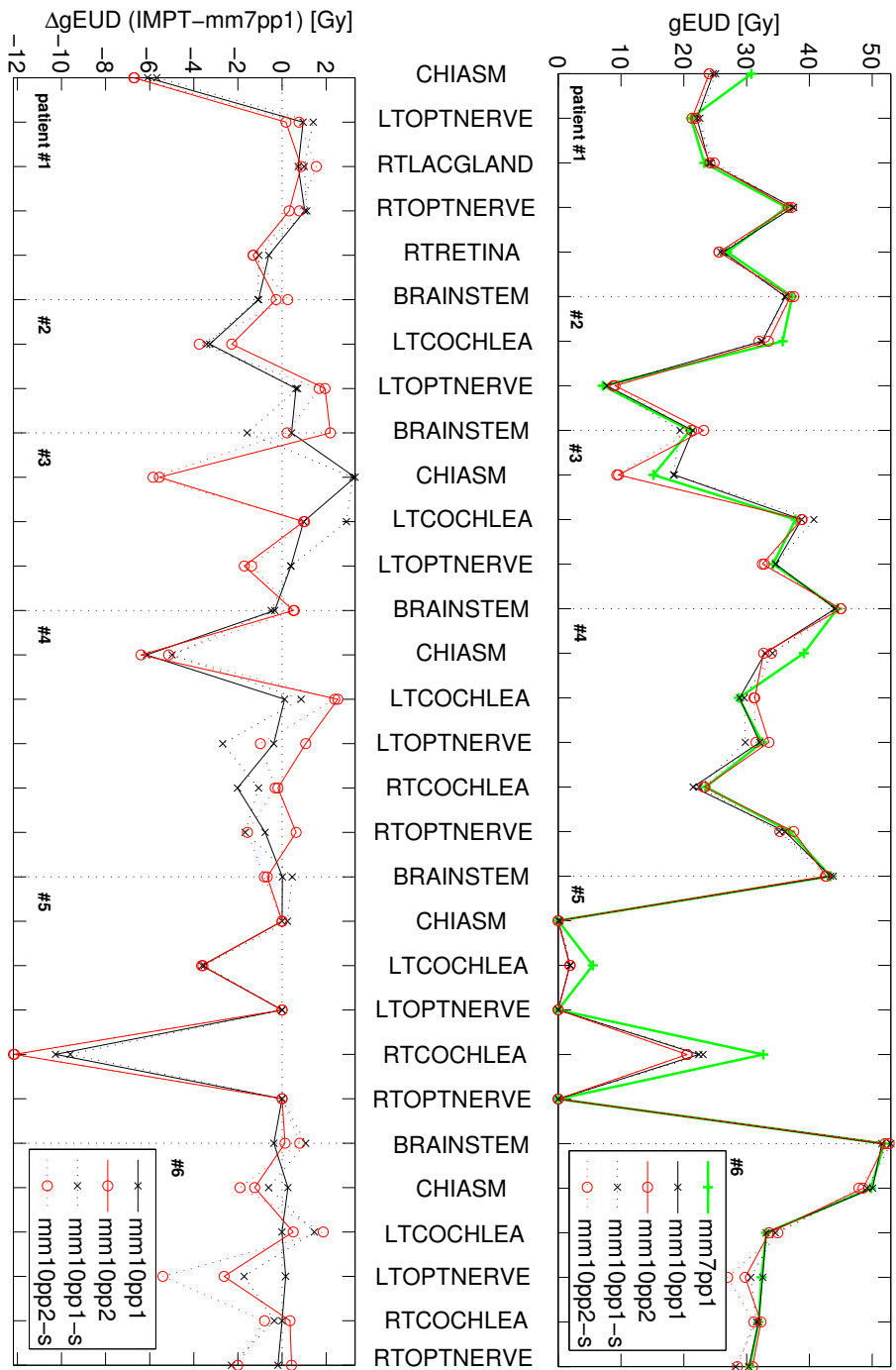


**Figure 2.18:** *Upper:* absolute generalized equivalent uniform dose (gEUD) for all target volumes versus target index. *Lower:* Differences in target gEUD of all plans with respect to plans I. Data points have been connected to guide the eye.

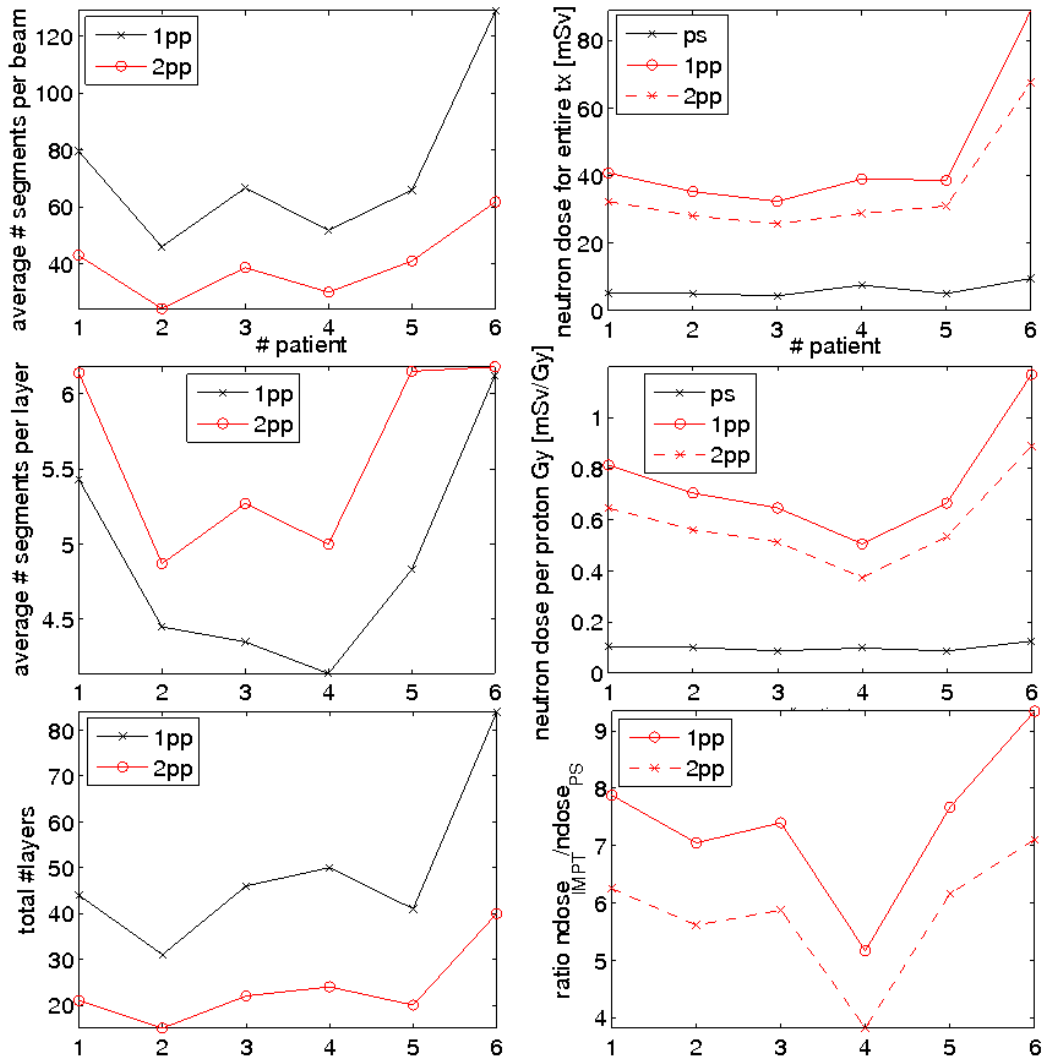


**Figure 2.19:** *Left:* Average number of segments per beam (upper) and layer (middle) as well as the total number of layers in the plans for all patients (lower) are plotted. *Right:* An estimate of the total neutron dose in mSv for the entire treatment course (upper), per delivered proton Gray (middle) and the ratio of IMPT to passive scattering values (lower). Values represent the neutron dose using a tungsten multileaf collimator, at a position approximately 75 cm off lateral from isocenter.

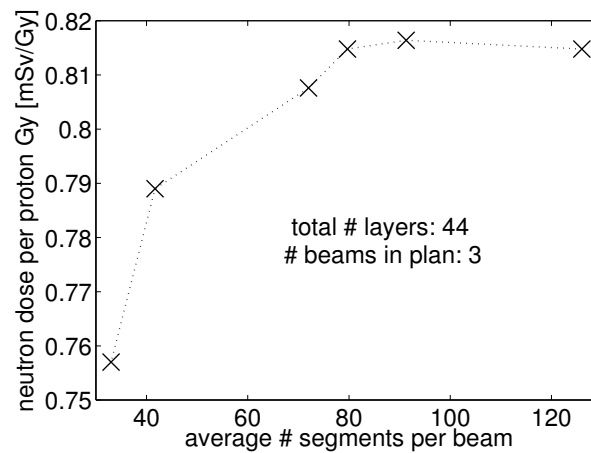


**Figure 2.20:** For one patient (# 1) plan IIs was sequenced with a range of numbers of segments per beam. Neutron dose in mSv per delivered proton Gray was estimated for each case.

## 2.2.4 Discussion

Without constraining the number of segments the quality of segmented dose distributions can be equal to the original. But, as expected, the quality of dose distributions decreases if the complex IMPT intensity maps are sequenced into fewer segments. Our optimization and segmentation approach resulted in acceptable treatment plans when using an average number of segments per beam of 73 and 40 for plans IIs and IIIs, respectively. Taking into account that typical intra-cranial IMPT plans consist of three to four fields this corresponds to 210 – 280 (IIs) and 120 – 160 (IIIs) to be delivered for any treatment fraction.

To put this into perspective we analyzed the step-and-shoot IMRT plans of 66 patients treated at our institute and planned with either the Corvus or the CMS XIO treatment planning system (33 patients each). All patients were treated with a Varian linear accelerator. The average number of segments per beam for Corvus and XIO was 50 and 22, respectively, while a typical plan consisted on average of 9 and 7 fields. This results in averages of 450 and 150 segments per treatment fraction. The average treatment times were 23 and 19 minutes for Corvus and XIO, respectively. These numbers indicate that it is technically feasible to deliver the segmented IMPT treatment plans IIs and IIIs.

Neutron dose for IMPT delivery is increased compared to passive scattering by a factor of 5 – 9 for IIs and 4 – 7 for plans IIIs. This translates into a maximum neutron dose per delivered proton Gray of about 1.2 mSv at a distance of 75 cm of isocenter under measurement conditions described in chapter 3.1. Neutron dose varies strongly with

beamline design. In the fixed horizontal beamline at the F.H.B proton therapy center measured neutrons dose are approximately an order of magnitude lower compared to our gantry beamlines. Here the beam is always scattered to a diameter of 25 cm regardless of the field size needed for treatment. For small fields this results in a large number of protons stopped very close to the patient in the aperture. In the fixed horizontal beamline (described in detail in chapter 3.1) the scatter diameter is 10 cm and therefore much less particles are stopped in the collimator per delivered proton Gray. The issue of beam efficiency through the collimator has recently been discussed by Hecksel *et al* [57].

NCRP 151 [58] reports on neutron doses per photon Gray for a variety of linear accelerator models and energies with values varying between 0 to 2 mSv per photon Gray at 1.4 m distance from the target. Usually IMRT applications utilize an energy of 6 MV. This is below the threshold for neutron production, and hence the secondary neutron dose is zero. Due to the increased number of monitor units in IMRT however, the scattered photon dose is significantly increased. Athar *et al* [59] reported that at relevant distances larger than 25 cm from the field edge IMRT dose is approximately 1 mSv per photon Gray.

Although an increase in neutron dose of a factor of 4 – 9 when applying IMPT compared to SOBP treatments is undesirable, the absolute neutron dose to the patients can be reduced to acceptable levels with careful beamline design. The neutron dose can be further reduced by optimizing the design of the collimator itself [60].

This study represents an initial feasibility analysis for MLC based IMPT. Further improvement of our results may be achieved by employing an optimizer specifically designed for the task of MLC delivery with the goal of minimizing the number of segments and neutron dose to the patient.

## Conclusion

Our preliminary study indicates the feasibility of segmenting IMPT intensity maps for treatment delivery by means of a multileaf collimator in a passive scattering proton therapy beamline. Loss in plan quality can be maintained at an acceptable level while reducing the required number of MLC segments. The increased flexibility in dose delivery has to be weighed against an increase in secondary neutron dose to the patient.

Since segmentation results in a requirement to deliver multiple small fields, for clinical implementation, a comprehensive study of small field dosimetry is necessary (Chapter 3.2).

# Chapter 3

## Experimental Studies

The properties of a collimator, geometry and material composition, influence the dose distribution. Exploring those properties is a necessary task on the way to implementation of a multileaf collimator for beam delivery.

Section 3.1 describes the most important features of a mini-multileaf collimator<sup>1</sup> in a proton therapy beamline, in comparison to custom milled apertures used routinely. An important part of those measurements are neutron doses for various field size, energies and airgaps. This data set served as the basis for neutron dose estimate in section 2.2

As mentioned in previous chapters small-segment delivery is very common to MLC based IMPT. Since charged particle equilibrium breaks down for smaller fields the dose at peak depth changes with field size. The relationship of peak dose versus beam aperture shape has to be known for accurate IMPT delivery. Section 3.2 contains a measurement set that will serve as a basis for monitor unit calculation.

### 3.1 The dosimetric properties of MLCs in a proton beam

#### 3.1.1 Introduction

The majority of proton therapy centers use a passively scattered beam [61] [62] in combination with a custom milled aperture and range compensator for final, per-field, beam shaping. Torikoshi *et al.* [63] previously published on the application of a custom

---

<sup>1</sup>Integra Radionics, Burlington MA

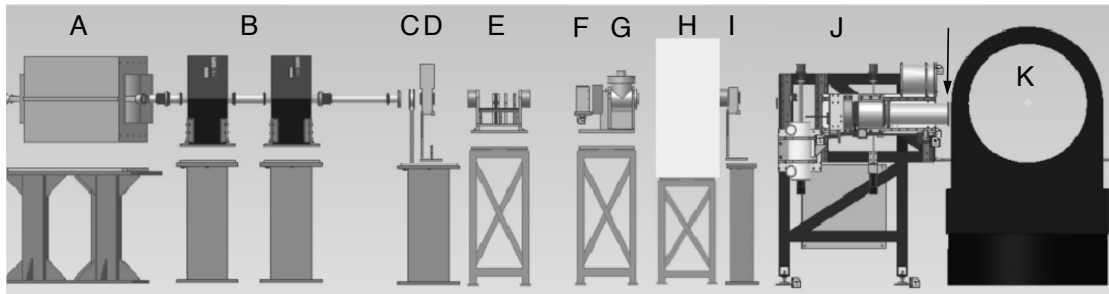


**Figure 3.1:** Side view of the STAR (STereotactic Alignment in Radiosurgery) beamline. From left to right: bending magnet (A), quadrupoles (B), ion chamber 1 (C), beam profile monitor (D), binary absorber system (BABS, E), range verifier (F), beam stop (G), neutron shielding (H), ion chambers 2 and 3 (I), nozzle stand with x-ray tube, cone and aperture (J), STAR patient positioner (K). The arrow indicates the position of the mMLC. Not to scale.

multileaf collimator in their carbon ion therapy beamline. It is used as final collimator for extra-cranial lesions, and has been commissioned for a layer-stacking [64] [65] technique. Layer-stacking has been applied to a handful of patients and has since been discontinued [66]. Ainsley *et al* [31] are employing Varian multileaf collimators in IBA gantry beamlines for conformal proton therapy for large targets.

This work investigates the usability of a mini-multileaf collimator (mMLC) in passively scattered proton beam therapy for intra-cranial lesions. The goal is to study the mMLC as a replacement for custom milled apertures. We use a commercial mini-multileaf collimator manufactured by Integra Radionics for which we explore the mechanical and dosimetric properties.

### 3.1.2 Methods

#### Beamline

Figure 3.1 shows a schematic drawing of the STAR (STereotactic Alignment in Radiosurgery) beamline. The beam direction in our intra-cranial beamline is fixed in the horizontal plane. The 5-degree-of-freedom patient positioner allows rotation and translation of the patient with respect to the beam isocenter. In combination with collimator rotation, our system has the necessary degrees-of-freedom to achieve any beam direction.

A proton beam of fixed initial energy (185 MeV) is degraded and scattered by a Binary ABsorber System (BABS, see Figure 3.2(a)) consisting of a set of ten lexan and

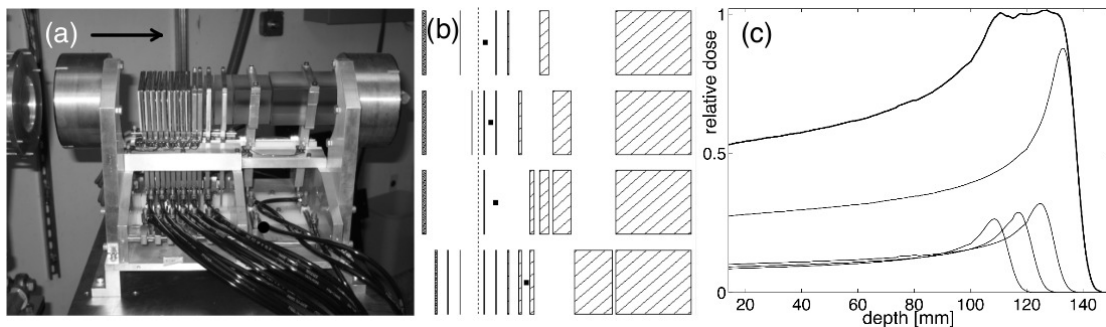


**Figure 3.2:** (a) The binary absorber system BABS consists of 5 lead and 10 lexan blocks. Brass apertures up- and downstream confine the beam laterally. (b) & (c) STAR produces SOBP's by consecutive delivery of pristine Bragg peaks. In the example in (c) an SOBP with a range and modulation of 13.5 cm and 3 cm is produced by a sequence of four pristine peaks. The black dot in (b) represents the virtual source position. The blocks symbolize those lead (left of dashed line) and lexan (right of dashed line) absorbers which are brought into the beam path to achieve the desired pullback and angular spread [56]

a set of five lead blocks. Within each set the thickness of a scatterer equals half the thickness of its upstream (lead) or downstream (lexan) absorber. Spread-out Bragg peaks are produced by the consecutive delivery of single pristine peaks of different range and weight, i.e. the dose is delivered range layer by range layer (Figures 3.2(b) and 3.2(c)). BABS scatters the particles to a constant field diameter of 10 cm, and degrades the initial energy to the desired treatment range between 2 and 19 cm in water and arbitrary modulation.

The large source-to-axis distance (SAD, 460 cm) minimizes the impact of the source size on dose, i.e. sharper penumbra and less pronounced effect of field size on output. The beamline is commissioned to deliver a continuous range of proton energies and modulations, allowing highly conformal treatment plans.

### MLC system

The mMLC was constructed for the geometry of a clinical linear accelerator (LINAC) with an SAD of 100 cm. The sixty-two tungsten leaves have a thickness of 73 mm and a width of 2.225 mm at the upstream and 2.517 mm at the downstream face. Physical aperture outlines formed by the mMLC measure up to 69 mm parallel to the direction of leaf motion and 54 mm perpendicular. Tongue and groove construction of 0.3 mm limits inter-leaf leakage while an additional step of 0.3 mm limits leakage between abutting leaves. The control software for the mMLC is provided by Integra Radionics and runs

on a Windows platform. The leaf positions for a treatment field are set according to an input file, which is created by an external application.

**Field Reproducibility** An important factor for mMLC treatments is the accuracy of the leaf motion. A rectangular shaped mMLC outline involving all leaves was set ten times, measuring the field dimensions with x-rays acquired by a digital panel .

**Field Shaping** The leaves are tapered perpendicular to their motion direction to sharpen the lateral dose fall-off for photons. Our beamline SAD of 460 cm results in a smaller beam divergence compared to a LINAC with an SAD of 100 cm. Thus, the downstream and upstream edges determine the field shape along and perpendicular to the leaf motion respectively. We therefore need to incorporate the geometry of the mMLC (taper and leaf thickness) and our beamline (SAD) into a leaf positioning algorithm. The beamline SAD as a function of range is obtained by measurements of lateral profiles in air at different distances from the source. The FWHM of these profiles was extracted and extrapolated to zero width, which corresponds to the virtual source position. Since the SAD varies with the type and amount of BABS material in the beam path, the SAD has to be measured for a set of ranges. To minimize dose-averaging, in-air profiles were measured with a mini-thimble ionization chamber with an active volume of  $0.0073 \text{ mm}^3$  constructed by Schreuder [67]. Given the SAD, the leaf settings for a field shape can be accurately calculated. The leaf positioning algorithm was written and explained in detail by Bangert [68]. In short, mMLC thickness and taper are considered by calculating leaf settings for two infinitely thin collimators located at the upstream and downstream edge of the mMLC. The above algorithm is applied to both, where the input contour is the projected original contour. The final leaf position is the most retracted of the two. All measurements are done with a 50% overlap of leaves and contour. The verification of the leaf-positioning algorithm includes proton beam measurements with radiographic film in air, for ranges of 4 cm and 18 cm, and a circular field shape of 5 cm diameter.

## Measurements

**Dose Distribution.** The leaf width ( $\approx 2.5 \text{ mm}$ ) and the mMLC taper influence the dose conformity, penumbral width, and scatter characteristics from the inner collimator walls. The differences between brass and tungsten, however, are not expected to produce a measurable difference. A possible difference in scatter might be reflected in a change of the peak-to-entrance ratio for small fields. We therefore measured lateral and depth doses for mMLC and brass aperture. Lateral doses were measured with Kodak XV film

placed at the center of SOBPs with ranges of 18 cm, 12 cm and 4 cm and modulation of 2 cm. Vertical and horizontal profiles through the spot centers were extracted and compared. The response of radiographic film can be non-linear in both dose and proton energy. To guarantee linearity, films were irradiated with no more than 30 cGy. This limit is the result from unpublished measurements investigating the dose response for a variety of energies. Monte Carlo simulations furthermore showed that the mean energy of protons in the penumbral region changes only for doses below the 50% level. We therefore use the 50-95% width to avoid impact of the energy response of film on our results. A PTW N31006 pin-point ionization chamber (active volume  $0.015 \text{ cm}^3$ ) was used for depth dose measurements in a Wellhoefer water tank for pristine Bragg peaks of ranges 4 cm, 12 cm and 19 cm and field diameters between 10 mm and 50 mm. Measurements of small proton fields are generally difficult. The ideal detector would have linearity in dose response, no energy dependency, and a small active volume to avoid dose averaging. The latter could affect our measurements for the smallest field sizes. Two-dimensional dose distributions for mMLC and aperture were obtained with radiographic film for 2 cm wide SOBPs of ranges 4 cm and 18 cm. The film was placed in the center of the SOBP. The effect of the leaf width on dose conformity was studied by means of  $\gamma$ -index analysis [69] of aperture and mMLC shaped dose distributions. For this test we used an irregular field shape forming a single beam as used in a clinical treatment plan. The dosimetric and spatial criteria were 2% of the global maximum dose and 1.5 mm, respectively.

**Proton Leakage, Neutron Production & Activation.** Measurements were performed to quantify equivalent dose, in Sievert per delivered proton Gray, to the patient due to leakage protons and secondary neutrons. Activation of the tungsten leaves was examined. The mMLC leaf thickness of 7.3 cm is twice that necessary to stop protons of our maximum energy of 185 MeV. Hence, proton leakage is expected only where leaves abut and not in between the leaves due to the tongue-and-groove construction and the taper. Radiographic film was placed in air at isocenter, and a dose of 16 Gy delivered with fully closed leaves. The shut-position of the leaves was altered such that leaves abut outside the field. We expect a higher neutron flux from tungsten compared to brass. Neutron measurements were performed with Bonner spheres (diameter 25.4 cm) placed in a variety of locations inside and outside the treatment room. To assess upper and lower limits of the neutron dose the experiment was conducted for pristine peaks with ranges of 4 cm and 18 cm, with fully closed collimators as well as different sizes of collimator openings while stopping the beam in a polyethylene block located at isocenter. The activation of the closed mMLC was measured over a 24 hour time period with a Geiger counter after the delivery of 16 Gy using a proton range of 19 cm.

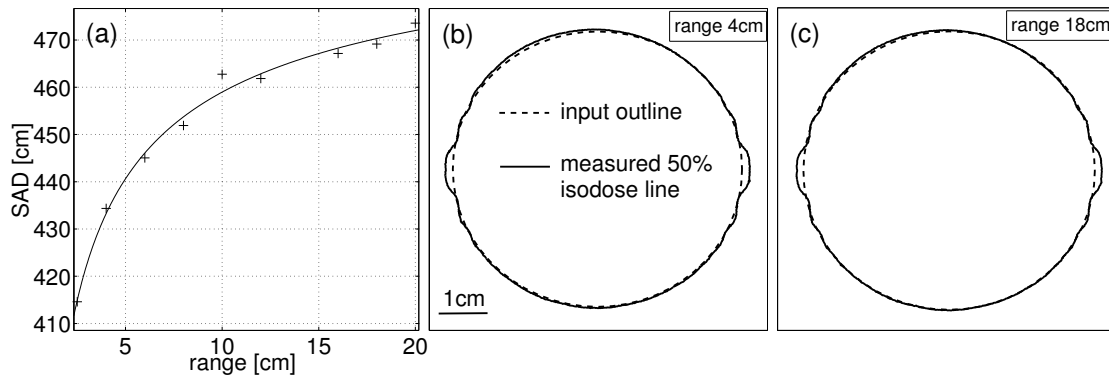


**Figure 3.3:** Due to the one-directional taper of the mMLC knowledge of the range dependent SAD is crucial to accurately shape treatment fields with the mMLC. (a) Results of our SAD measurements, the solid line is a fit to the data. (b) & (c) Film measurements of proton dose distributions in air at isocenter (airgap 43 cm) for  $R=4$  cm and  $R=18$  cm, respectively. The 50 % isodose line is printed solid, the input field shape (in this case a circle of 5 cm diameter) dashed.

### 3.1.3 Results

#### MMLC

**Field Reproducibility.** The repeated setting of rectangular collimator openings showed that the mMLC leaves reposition within a maximum uncertainty of 0.1 mm, i.e. the measurement uncertainty (the resolution of the digital panel).

**Field Shaping.** Figure 3.3(a) shows the result of our SAD measurements. We expect scattering to smooth the ragged collimator outline. Even in air, the scatter introduced in BABS is sufficient to converge the mMLC outline at the 50 % isodose line to the expected field outline. We thus compare the expected field shapes in-air to validate our leaf positioning algorithm. Figures 3.3(b) and 3.3(c) show the proton dose distributions in air for ranges of 4 cm and 18 cm, respectively, when aiming for a circular field of 5 cm diameter. At the field edges the influence of the leaf width on conformity is visible; in transverse direction the input contour is reproduced within half a leaf width. In all other areas the ragged outline of the mMLC fields is washed out by scattering and agrees well with the input contour. This is more so the case with increasing depth in the patient, improving the conformity of the dose distribution.

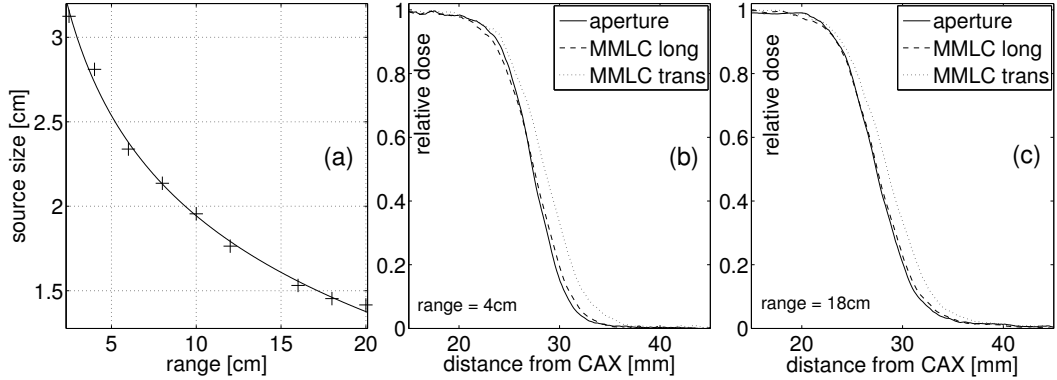


**Figure 3.4:** (a) Virtual source size ( $\sigma$ ) versus range. (b) & (c) Transverse and longitudinal lateral profiles for brass aperture and mMLC for ranges of 4 cm (b) and 18 cm (c) and a field of 5 cm diameter.

**Table 3.1:** Lateral 50–95 % widths of dose profiles through the center of circular radiation fields (in mm). For the MMLC transverse and longitudinal penumbra are given but averaged for the brass aperture.

range [cm]	brass aperture	mMLC long	mMLC trans
4	4.19	4.76	5.40
12	4.04	4.28	4.61
18	5.13	5.44	5.88

## Dose Distribution

**Lateral Profiles.** Two factors determine the width of the lateral fall-off: virtual source size and in-patient scatter. For low proton energies the source size dominates, while for deeper ranges multiple Coulomb scattering, MCS, in the patient contributes most to the spatial spread of the proton beam. Figure 3.4(a) displays the measured virtual source size versus range in water.

We measured lateral profiles to evaluate penumbral widths. Table 3.1 compares lateral 50-95% widths obtained for mMLC transverse (perpendicular to leaf motion) and longitudinal directions, and the brass aperture averaged over both directions. The penumbra is large at low energy due to the source-size increase, minimal at medium ranges as in-patient scatter and source-size are small, and is dominated by MCS in the patient at high range.

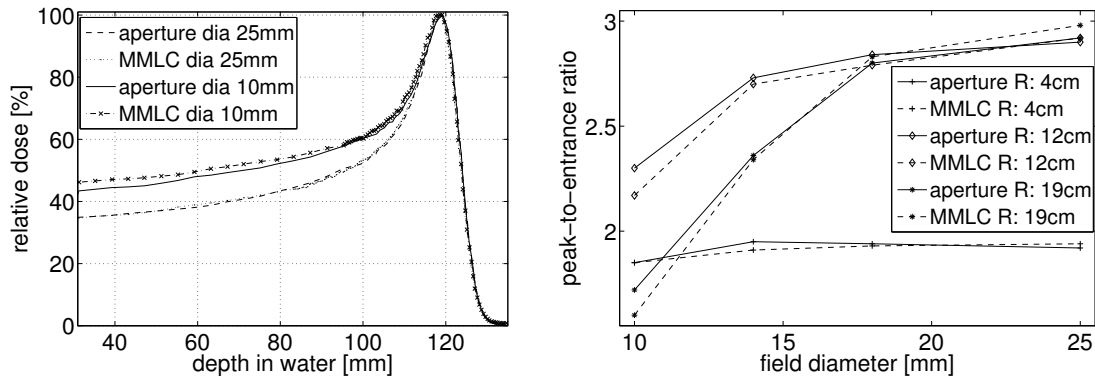


**Figure 3.5:** *Left:* Depth dose curves for field diameters 25 mm and 10 mm,  $R=12$  cm. *Right:* Peak-to-entrance ratios versus field diameter for  $R=4, 12, 19$  cm.

The finite leaf width results in a broader lateral fall-off for the mMLC by 0.2 mm to 1.2 mm (Table 3.1). The difference between transverse and longitudinal penumbra for the mMLC is clearly visible, the 50-95% width in longitudinal direction (no taper) is 0.5 mm smaller than perpendicular to it. The lateral profiles in the longitudinal direction (Figures 3.4(b) and 3.4(c)) show that the aperture and mMLC profiles agree within a maximum deviation of 0.6 mm. Those differences decrease with depth. We kept, for practical reasons, the airgap constant at 30 cm. In clinical practice brass apertures can be brought very close to the patient ( $\approx 2$  cm), while the mMLC will be positioned at a larger distance to avoid collisions ( $\approx 20$  cm). Due to the large SAD this only results in a minor additional difference in the penumbra of a few tenths of a millimeter (if no range compensator is present).

**Depth Doses.** Figure 3.5(a) shows central axis depth dose curves measured for mMLC and brass aperture for  $R = 12$  cm and field diameters of 25 mm and 10 mm. The difference in entrance dose between the 25 mm and 10 mm diameter aperture is due to lateral charged particle disequilibrium. A summary of all measured peak-to-entrance ratios for various ranges and field diameters is given in Figure 3.5(b). The data show no significant difference in range ( $\leq 0.5$  mm), width ( $\leq 0.5$  mm) and distal fall-off between mMLC and aperture shaped depth doses. There are, however, slight differences in the peak-to-entrance ratio for 10 mm wide fields of about 4% for 12 cm and 19 cm ranges. This might indicate changes in collimator scatter due to material and geometry differences of the two collimators. Measurement uncertainty, however, is increased for such small fields.

**Planar Dose Distributions.** Figure 3.6 shows the  $\gamma$ -index analysis for a patient

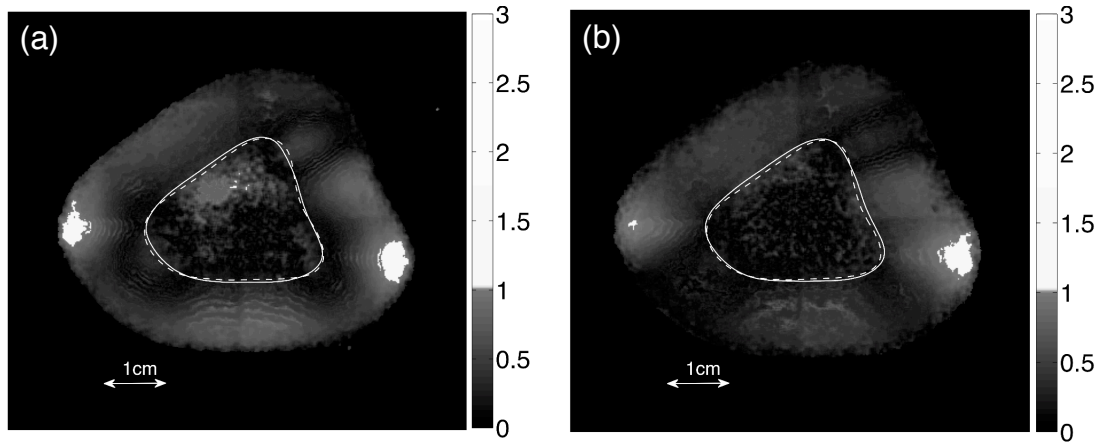


**Figure 3.6:**  $\gamma$ -index images comparing aperture and mMLC shaped dose distributions for a realistic treatment field. The space and dose criteria were 1.5 mm and 2 %, respectively. Leaf motion direction is up-down. Dashed (aperture) and solid (MMLC) outlines represent the 90 % isodose line. (a)  $R = 4$  cm, (b)  $R = 18$  cm.

field with ranges of 4 cm and 18 cm and 2 cm modulation. The criteria (2% of the central axis dose, and 1.5 mm) are met everywhere except in the field edges.

### Leakage/Transmission

**Proton Leakage.** The developed and digitized film did not show any dose response. Since doses above  $\approx 5$  cGy produce a visible response on the film, we conclude that, given the delivered dose of 16 Gy, interleaf leakage is smaller than 0.3 %.

**Neutron Production.** We measured a neutron dose of 0.03 mSv/Gy to 0.13 mSv/Gy for a closed brass aperture and a Bonner sphere located at isocenter, and 0.04 mSv/Gy to 0.23 mSv/Gy for the mMLC (Figure 3.7, left). These numbers are on the very low end of the range of data reported in the literature. References [70] [71] [72] [73] [74] [75] [76] [77] [78] report on previous simulations and measurements of neutron doses at various proton therapy institutions. Measurements in our double-scattering gantries using the same detectors and a similar setup showed a neutron dose of 2.5 mSv/Gy at isocenter, which is 10 times more than detected with the mMLC. Our results (Figures 3.7 and 3.8) furthermore confirm the expected higher neutron doses in the tungsten mMLC (by a factor of 1.5 to 1.8) compared to brass apertures. For the mMLC the typical airgap is  $\approx 20$  cm and  $\approx 2$  cm for the brass apertures. Comparing neutron doses for those airgaps (see Figure 3.7), one finds that in a clinical situation, because of the larger airgap, the neutron dose would actually be less for the mMLC ( $\approx 0.32$  versus  $\approx 0.45$  mSv/Gy for R

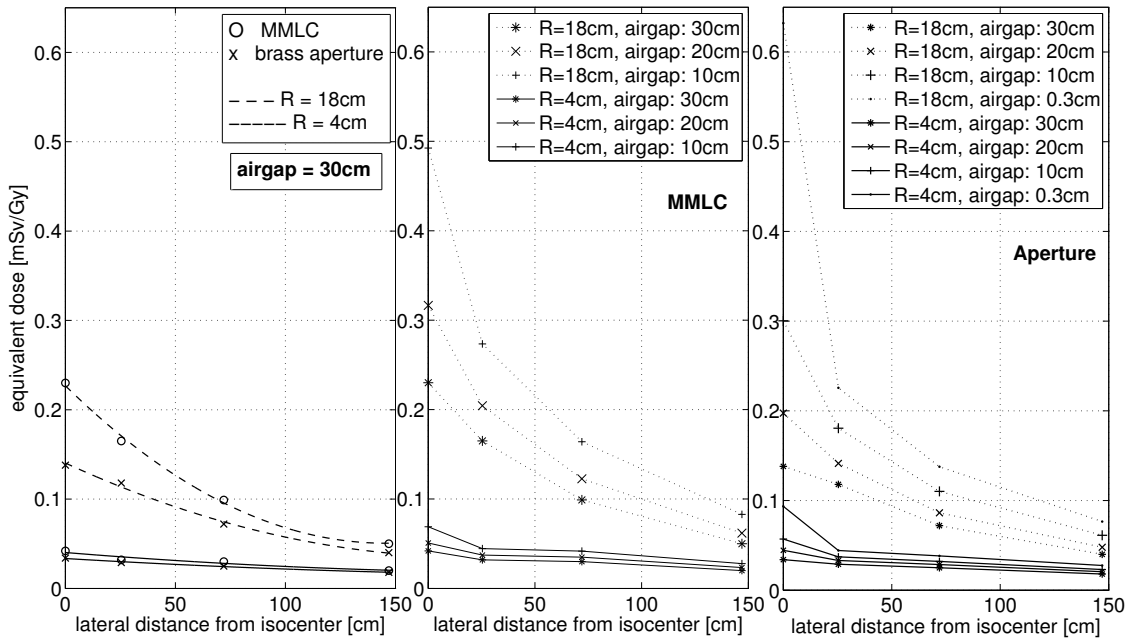


**Figure 3.7:** Neutron dose per delivered proton dose versus lateral distance from isocenter. The beam was fully blocked by the collimator. *Left:* mMLC and brass aperture for  $R=4$  cm and  $R=18$  cm, airgap = 30cm. *Center:* mMLC for  $R=4$  cm and  $R=18$  cm and various airgaps. *Right:* Brass aperture for  $R=4$  cm and  $R=18$  cm and various airgaps.

= 18 cm). The out-of field dose in such a situation would be approximately equal in such a case. Figure 3.8 shows a clear relation between collimator opening and neutron dose. At a distance of 70 cm lateral to isocenter, the neutron counts are reduced by 40% for the mMLC and 17% for the brass aperture when using the maximal field opening. In this case the proton beam was stopped in a block of polyethylene, hence the measurements include neutrons produced in the plastic.

**Activation.** The mMLC was monitored over a 24-hour period after the delivery of 16 Gy (Figure 10). A selfshielding effect of the mMLC is visible in Figure 10(a). The activity at 1 m distance from the downstream side of the mMLC (dashed line) is lower than at the same distance at a 90 degree angle to the beam direction. As even our maximum energy protons penetrate only to half the leaf thickness, the remaining 3.5 cm of tungsten act as shielding. Figures 3.9(b) and 3.9(c) simulate two days of delivery of 1Gy every 15 minutes for 10 hours a day, based on our measurements. At a distance of 1m downstream of the collimator the activation reaches its maximum at  $\approx 6 \times 10^{-4}$

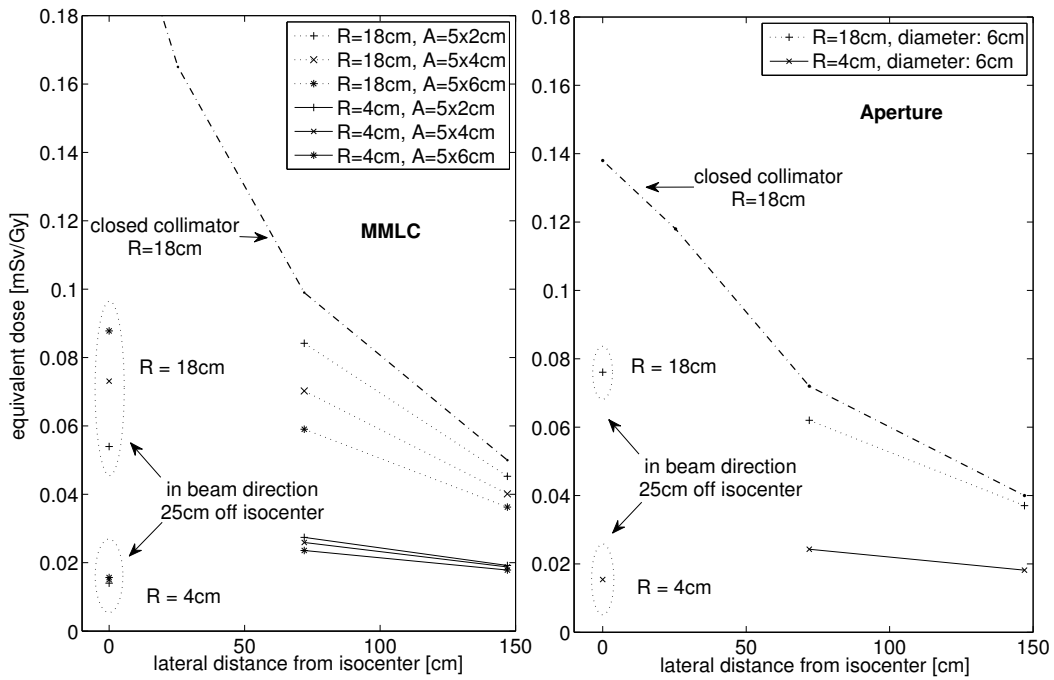


**Figure 3.8:** Influence of collimator opening on neutron dose. For comparison we included the data for a closed collimator at 18 cm range. *Left: mmC Right: brass aperture.*

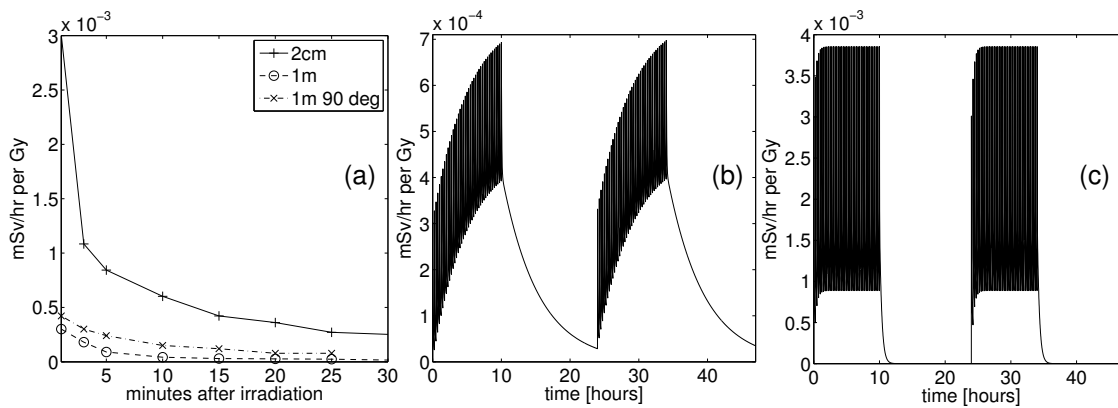


**Figure 3.9:** (a) Activation of the mMLC per delivered Gray as measured with a Geiger counter at various locations. *Solid line: 2cm downstream of leaves, dashed line: 1m downstream, dash-dotted line: 1 m distance to mMLC at a 90 degree angle to the beam.* (b) & (c) Simulation of the mMLC activity over the course of two treatment days, assuming the delivery of 1 Gy every 15 minutes for 10 hours per day. (b) As measured at 1 m distance of the mMLC (in beam direction) (c) measured at 2 cm distance to the leaves.

mSv/hr, at 2 cm distance at  $\approx 4 \times 10^{-3}$  mSv /hr. After the 14 hour break the activation was at background level  $\approx 0.5 \times 10^{-4}$  mSv/hr.

### 3.1.4 Discussion

Torikoshi et al. have reported on their custom-designed multileaf collimator for extracranial treatments [66]. Their MLC consists of 6.5 mm thick steel leaves, and the device is used as final collimation in their carbon ion therapy beamline. For increased lateral conformity, intra-cranial lesions are still treated with custom milled collimators. We validated the applicability of a commercially available mMLC for use in intra-cranial proton therapy. The mMLC has been specifically designed for use in photon linear accelerators; the choice of leaf material was based on attenuating photons, and the leaves are tapered according to an SAD of 1 m. Our dosimetric verification, however, shows only small differences in the dose distributions as obtained with brass apertures and the mMLC. High-dose regions agree, differences are confined to areas below the 50 % isodose level, which is a direct consequence of the ragged outline of the mMLC shaped field. This raggedness decreases with depth due to an increase in multiple Coulomb scattering. When forming outlines with MLCs the conformity is limited by the leaf width. In transverse direction the input shape will only be reproduced within half a leaf width. Depending on the target shape it might be beneficial for the dose distributions to close the leaf pair at the field edge. The consequence of the leaf width on penumbra amounts to a 1.2 mm increase in transverse direction for the worst-case scenario of very shallow ranges. In the majority of clinical situations these limitations should not have a clinically significant impact. Especially in composite dose distributions of multiple beam directions the penumbral width of a single proton beam becomes less important. It is, however, important to note that there might be an appreciable worsening in situations with thick range compensators considering the large airgap. Differences between mMLC and brass apertures in depth dose characteristics were found to be negligible.

Considering neutron production tungsten is not an optimal material for a proton beam collimator. Compared to brass our measurements show an increase in neutron dose of up to a factor of 2 when using the mMLC. In clinical situations (large airgap for mMLC), however, the in-field neutron dose is actually higher with brass apertures. Neutron measurements in our beamline furthermore show 10-20 times lower doses than in our gantry systems. Final collimators have the largest contributions to the neutron dose to the patient in the gantries and STAR. The proton beam in STAR is scattered to a 10 cm field diameter and in the Gantry rooms to 25 cm, i.e. a six times larger area over which protons are stopped close to the patient. STAR also has a larger SAD (4.6 m versus 2.3 m) and extensive neutron shielding between the scatterers and the patient.

Hecksel *et al* [57] have recently reported in detail on the relationship between neutron dose and field size. Their findings were reproduced analytically by Anferov [79].

Note that our measurements were performed using single pristine peaks; the delivery of SOBPs increases the number of Monitor Units, and hence the neutron dose increases (for example, to achieve an SOBP of 8 cm modulation, the number of MU increases by a factor of 2.2). Another critical factor is the quality factor to be used. We follow Mesoloras [77] who uses a quality factor of 5.9 according to Monte-Carlo simulations of Jiang [75]. Close to the aperture edge Wroe [78] measured a quality factor of 2, increasing to 7 further away from the radiation field. Hence, compared to Wroe, we overestimate our values at isocenter by about 300% and underestimate the out-of-field values by about 15%. This emphasizes the difficulties of comparative neutron measurements and their analysis. References [70] – [78] report on measurements and simulations in various beamlines.

It is well known that the energy response of Bonner spheres does not allow highly accurate measurements of neutron fluxes with spectra as they are produced in proton therapy beamlines. Cascio *et al* [80] has investigated the energy response of Bonner Spheres and measured neutron spectra in detail. The upper energy threshold for neutrons detectable with these detectors was  $\approx 100$  MeV. Data measured in beam direction therefore does not include dose from high-energy neutrons present at this position. Cascio *et al* furthermore showed that the energy spectrum for off-axis measurements is shifted towards lower energies than in beam direction. Neutron measurements done lateral of the central axis are therefore much less influenced by the energy cut-off of the detector.

At our institution Bonner spheres have for a long time been the standard detector for neutrons. Although there are deficiencies when using these detectors, it was important for the experiments performed for this thesis to allow a comparison of the neutron dose in our gantry beamlines with doses measured in the STAR beamline. This was accomplished by using a similar experimental setup as previously done at our facility.

Measurements performed by Wroe *et al* [81] in our beamline using solid state microdosimeters confirmed the large reduction we found in neutron dose in STAR compared to the gantry beamlines.

### 3.1.5 Conclusion

The main dosimetric characteristics of the Radionics mMLC were investigated in comparison to custom brass apertures. Lateral penumbra was found to be slightly wider, depth doses very similar. Field conformation was acceptable. Neutron dose was clearly increased with the tungsten collimator, but due to beamline properties still lower than data gathered in other beamlines. Activation of the leaves was not an issue.

The geometric properties and material choice of the mMLC can be optimized further to improve dosimetric characteristics. But even though the device was specifically designed for a photon linear accelerator, we conclude that it can be safely and effectively used for field shaping in our proton beamline.

## 3.2 Dosimetry of small Fields

### 3.2.1 Introduction

The presented measurements were performed using brass apertures rather than the mini-multileaf collimator introduced in the previous chapter. Brass apertures allowed the measurement of larger fields, and the collection of data in the two remaining proton beamline designs available at our institution. The aim of the study was to gather data in all beamlines for a wide range of setup parameters, and to possibly derive a generalized formalism for field size correction of the output in proton therapy. In addition, the presented data set is applied for routine clinical use.

The output factor (i.e. dose per monitor unit) in passively scattered proton therapy depends on the beam range and modulation. It therefore needs to be determined for each treatment field, either by measurement or by model. After eight years of experience with our equipment we now are able to confidently model the output factor in all beamlines, eliminating the need for daily field calibrations and freeing up valuable resources [82] [30]. Output models were established based on a set of data measured for a large set of ranges and modulations, using standard conditions for the experimental setup and machine settings [30]. In particular, the models for all three beamline designs are based on measurements obtained with a standard aperture size, and no range compensator. This means the effect of patient specific hardware is neglected - a widely accepted concept in proton therapy [83]. It is, however, well known that the output for small fields decreases due to charged particle disequilibrium. It was therefore essential to quantify the effect of the field size on the output factor to validate dose calculations of our treatment planning system for small treatment fields. Our treatment planning system uses a pencil beam algorithm for dose calculation. The loss of fluence on the central axis can be described applying the pencil beam formalism [84]. Solving the dose integral on the central axis and normalizing to the open field dose one obtains:

$$F(r, \sigma_{tot}) = 1 - \exp\left(-\frac{r^2}{2\sigma_{tot}^2(z)}\right) \quad (3.1)$$

with  $F$ , the normalized output factor,  $r$  the field radius and  $\sigma$ , the standard deviation of the angular distribution at depth  $z$ . The angular distribution is determined by the virtual source size and the scatter in range compensator and patient:

$$\sigma_{tot} = \sqrt{\sigma_{source}^2 + \sigma_{rc}^2 + \sigma_{patient}^2} \quad (3.2)$$

The presented measurement series assess how accurately our dose calculation algorithm can predict the observed field size dependence of the output factor. We show the necessity to correct for the reduction of the output outside of the treatment planning system, and describe the method currently used at our facility.

### 3.2.2 Methods

Our beamlines differ significantly in their design. The dedicated intra-cranial stereotactic beamline (STAR) employs a binary absorber system to spread and degrade the beam. The two IBA gantry beamlines use a double scattering system, with a combination of fixed scatterers, range modulator wheels and second scatterers. Our fixed horizontal eye treatment station uses single scattering and range modulator wheels to create spread-out Bragg peaks (SOBP). For this work output factors, i.e. dose in cGy per monitor unit MU, have been obtained in each of the three beamlines, for an extensive set of field sizes and proton energies. The position of the measurement point (in the following referred to as POI - point of interest) is the same as the calibration point: on the central axis in the center of the SOBP high dose region, aligned with isocenter. Doses were calculated for the STAR beamline, reproducing the experimental setup (i.e. range, modulation, aperture size, detector position, air gap) in the CMS XiO treatment planning system, using the dose calculation algorithm as described by Hong *et al* [84]. The results were compared to measurements. In the following we briefly describe the properties of the beamlines and the series of measurements obtained in each.

**The fixed stereotactic intra-cranial system (STAR).** This system was described in detail in Chapter 3.1.2. In short, it is a single scattering system with a fixed initial proton energy and a large source-to-axis distance varying between 400 and 470 cm and a source size between 2.5 and 3.5 cm. Fields with diameters between 1.2 cm and 10 cm are treated. The final collimating custom brass aperture is mounted in a narrow aluminum

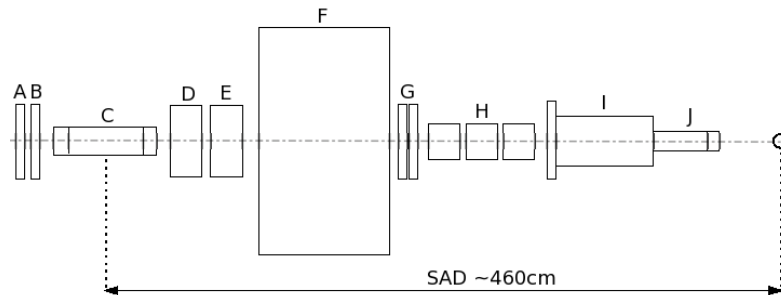


**Figure 3.10:** Sketch of the STAR beamline. A: monitor chamber 1. B: beam profile monitor. C: Binary Absorber System. D: range verifier. E: beam stop. F: neutron shielding G: monitor chambers 2 & 3. H: aluminum tubes. I: nozzle. J: cone with patient specific hardware.

cone. We can choose between two cone sizes, 6 cm and 10 cm diameter. A sketch of the beamline is depicted in Figure 3.1.2, and for better comparison to the remaining two systems in a simplified form in Figure 3.10.

**Gantry beamlines.** Ranges in the gantry beamlines (see Figure 3.11) vary between 4.6 cm and 25 cm, modulations between 1.5 cm and 25 cm. This range interval is sub-divided into seven treatment options, each characterized by the combination of range modulator track and second scatterer in use. This gives each option a unique behavior regarding output as a function of range and modulation. For the treatment of prostate we use an eighth treatment option for ranges up to 29 cm, but we excluded this option from the presented measurement series. The maximum and minimum field diameters are 25 cm and 1.2 cm, respectively. The beamlines source-to-axis distance ( $SAD \approx 227$  cm) and virtual source size (2 cm - 4 cm) are range-dependent.

The patient specific hardware is mounted in a heavy cone consisting mainly of brass, the snout (3.11, item G). Three snout sizes are available, limiting the field diameter to 12 cm, 18 cm or 25 cm. The beam, however, is always scattered to the maximum field size of 25 cm diameter, independent of the snout size in use. For the treatment of small fields ( $\leq 4.5$  cm) a brass adapter (HiHat) can be mounted to the 12 cm snout to allow closer proximity of the aperture to the patient. This adapter aperture reduces the beam to a diameter of 4.5 cm. A custom aperture is mounted on top of the adapter for final collimation. A more detailed description of the beamline design can be found in reference [82].

**The eye beamline.** The initial proton energy entering this beamline is constant

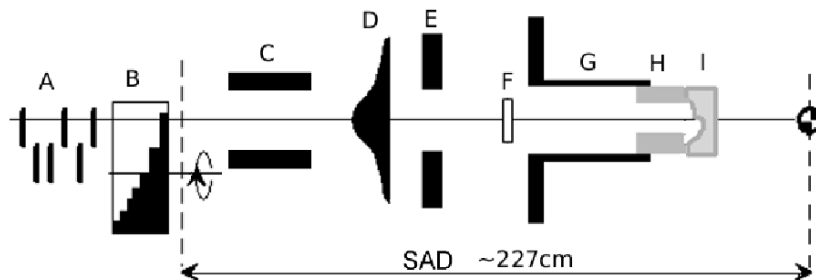


**Figure 3.11:** Sketch of the gantry nozzle. A: fixed scatterers. B: range modulator wheel. C & E: scanning magnets. D: second scatterer. F: monitor chambers. G: snout. H & I: patient specific hardware.

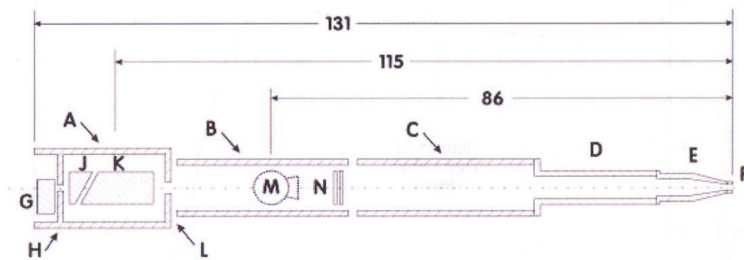


**Figure 3.12:** Sketch of our eye treatment station. A-D: brass cylinders constituting the nozzle. E: tapered brass snout. F: final field defining aperture. G: modulator wheel. H: collimator. J: adjustable thickness degrader. K: fixed thickness degrader. L: collimator. M: x-ray tube. N: ion chambers.

at 160 MeV. The particle energy is degraded by the fixed and variable degrader (Figure 3.12, right: J & K) to ranges in water less or equal to 4 cm. Spread-out Bragg peaks of up to full modulation are created by a library of modulator wheels. The majority of treatment fields are no wider than 28 mm in diameter; the minimum field size treated is 10 mm.

In the gantry beamline and in STAR a 1D-translational water phantom is used in combination with a PTW N31006 pinpoint ionization chamber (active volume  $0.015 \text{ cm}^3$ ) for performing a series of output measurements for a variety of ranges and field sizes. Alignment of the translational axis with the central axis of the proton fields was achieved by using the beamline X-ray system with the ion chamber both in the front and the back of the water phantom. Lateral alignment was optimized by maximizing the measured output for an 8 mm diameter field, while iteratively translating the water phantom in both lateral directions. Gantry beamline measurements included one range in each option 1-7 (5.2-22.4 cm). In STAR we covered five ranges between 5 cm and 18 cm. The

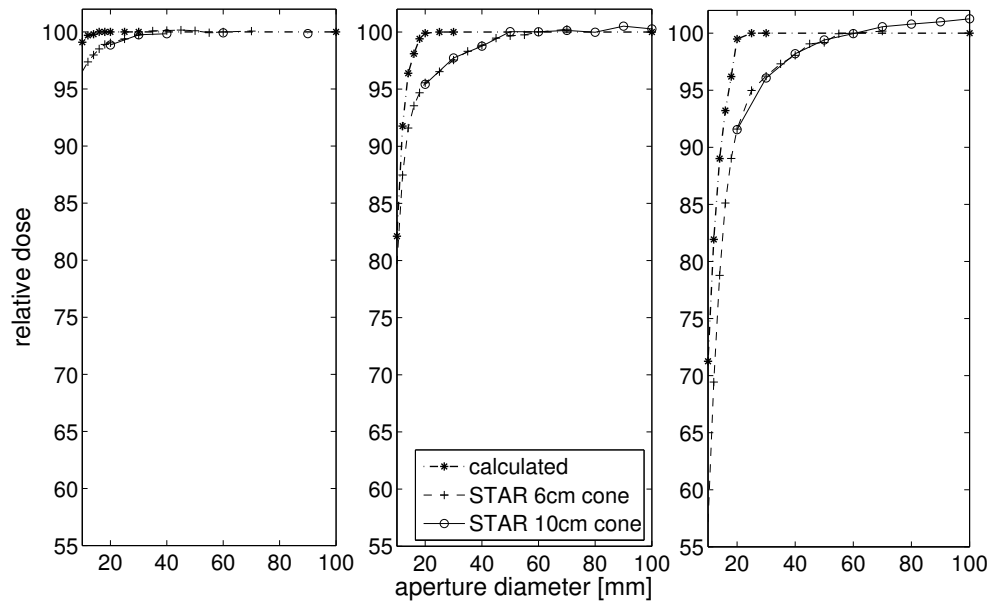


**Figure 3.13:** Calculated and measured doses at the center of a 2cm wide SOBP for the STAR beamline for ranges of 5 cm (left), 12 cm (middle) and 18 cm (right). Measured curves are normalized to the dose measured at 60 mm aperture diameter—the standard aperture size for field calibrations. Measurements were obtained with small (crosses) and large (circles) cone. Calculated values are indicated with a star symbol.

detector was placed in the center of a 2 cm wide SOBP. The data in the eyeline were obtained with a diode (active area  $\approx 1 \text{ mm}^2$ ), using a pre-absorber system to bring it to the correct depth. The mount of the device only allows fine-adjustment of the vertical position of the detector, hence there is small uncertainty in the alignment in horizontal direction ( $\leq 1 \text{ mm}$ ). We measured outputs for 3.2 cm and 2.7 cm ranges.

### 3.2.3 Results

#### Measurement versus calculation for the STAR beamline

Figure 3.13 shows a comparison of measured and calculated doses at SOBP center for ranges of 5, 12 and 18 cm in the STAR beamline. Since our output model is based on measurements with a field of 60 mm diameter and the 6 cm cone the curves were normalized to the output obtained at this reference field size.

The choice of normalization point (i.e. field diameter and cone size) is a clinical one and results in a shift of the curves. Regardless of the choice of reference condition,

some statements can be made regarding the general shape of our results. Relative to the largest field diameter the calculation overestimates the dose in the knee region. Beyond the knee, calculated doses reach a constant value. The measured data level off only for much larger field sizes for the ranges of 5 cm and 12 cm, and not at all for a range of 18 cm. The general  $(1 - \exp)$  - shape of the calculated curves does not hold for the measurements. It is important to note that this behavior cannot be explained by an error in the source size used for the dose calculation. Even when trying to adjust to fit the experimental values, our results cannot be described by Equation 3.1 for medium and deep ranges. (Nor is it advisable to change for this purpose, since that would also alter the calculated penumbral width.) As we cannot rely on the dose calculation for the output of small fields we chose to correct for the field size effect outside of our treatment planning system by applying a correction factor to the modeled output. In order to explain our observations and possibly improve future dose calculation algorithms the data set was extended to investigate the effect for the gantry and eye beamlines.

### Measured output versus field size for all three beamlines

The results are plotted in Figures 3.14 - 3.16. Since the output levels off to a constant value only for shallow ranges, one has to choose a normalization point for the curves. Our choice is the standard calibration field diameter for each beamline (28 mm for the eye beamline, 60 mm and the small cone for STAR and 120 mm and the 12 cm snout in the gantry beamline).

The projected source size in STAR is relatively small due to the long SAD. We therefore observe less of a field size effect in this beamline (Figure 3.14) than in the gantry beamline (Figure 3.15). In both systems, however, we measure a further increase in dose for field sizes for which lateral equilibrium is established, and no more change expected. This additional effect is more pronounced for increased ranges. In the gantry beamline, for example, we observe a 4.2 % increase in output between 40 mm and 120 mm field diameter when  $R = 22.4$  cm. For  $R = 13.6$  cm this is only 1.4%, while the curve flattens out at a field diameter of 70 mm. The effect of the field size on output is least pronounced in the eye treatment system (Figure 3.16). Due to the small  $\sigma_{tot}$  in shallow proton beams lateral particle disequilibrium only has a significant impact for fields with diameters less than 8-10mm. There is a further, shallow linear increase of 0.8 - 1.3 % per cm field diameter (range-dependent) beyond the knee, where constant output is expected. In short, the measurements in the eye treatment system confirmed

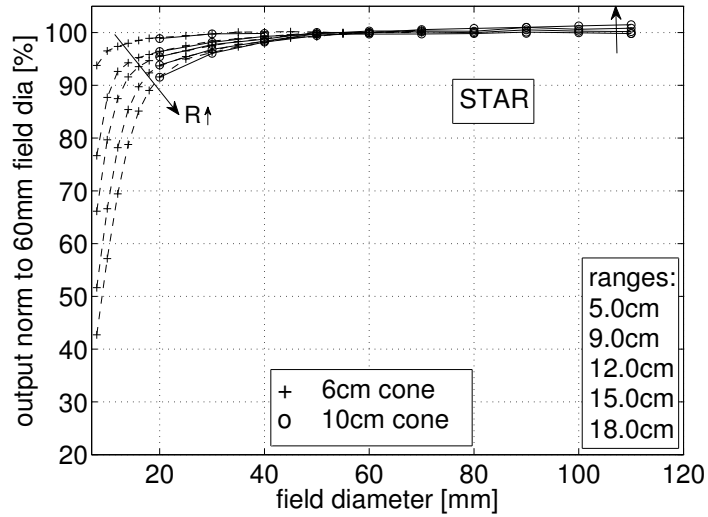


**Figure 3.14:** Output measured with a pinpoint ion chamber (PTWN31006) in STAR. Normalized to the value for our standard calibration aperture (6 cm diameter). The arrow marks the direction of increasing range.

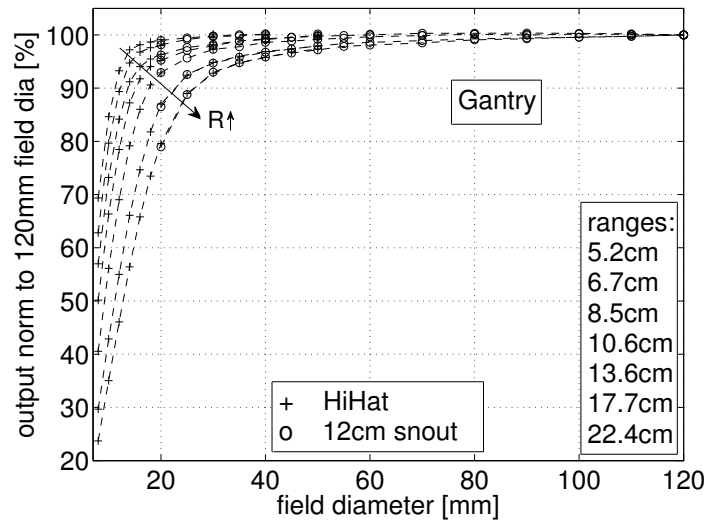


**Figure 3.15:** Output measured with a pinpoint ion chamber (PTWN31006) in the Gantry beamline. Normalized to the value for our standard calibration aperture (12 cm diameter). The arrow marks the direction of increasing range.

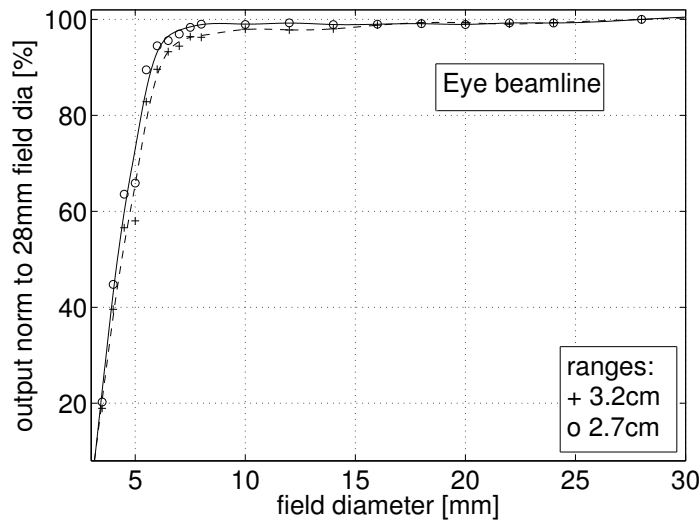


**Figure 3.16:** Measurement obtained with a diode in the eye beamline. All outputs are Normalized to the value for a 28 mm diameter aperture.

the observation of increasing output for large field sizes. However, since the magnitude of the effect is small for clinically applied field sizes (10 mm in diameter) field size effects for eye treatments were deemed negligible. In clinical practice we do not apply field size correction factors to the modeled output for the eye beamline. Seeing that these basic measurements showed the same trend in all beamlines (i.e. change in output for large fields) additional measurements were performed to explore the nature of the influence of field size on output.

### Effect of snout size, second scatterer, airgap and distance between POI and distal 90%

Data obtained at the gantry beamline and at STAR showed no dependence on the snout or cone used (12 cm with HiHat adapter, 12 cm, 18 cm and 25 cm snouts for gantry nozzle, 6 cm and 10 cm cone for STAR, Figures 3.14 and 3.15 and Table 3.2). This rules out an impact of scatter off the snout walls. Gantry beamline measurements with an open field and the 18 and 25 cm snouts showed no further increase in output compared to the 120 mm diameter fields (Table 3.2). In the gantry system we then measured the output of a 20 mm diameter field relative to 120 mm field,  $\Psi_{\varnothing 20/120}$ , to explore the influence of second scatterer, distance of the point of interest to distal 90% as well as the airgap. The purpose is to find the magnitude of the impact of those parameters on the relation of relative output versus field size. The value is a good indicator for this study

range [cm]	aperture diameter [mm]	12 cm	18 cm	25 cm
5.2	20	99.0	99.5	99.6
	40	100.0	99.9	100.3
	60	100.0	100.1	100.6
	180 (open)		99.7	
	250 (open)			100.3
10.6	20	95.1	94.7	94.8
	40	99.1	98.9	99.3
	60	100.0	99.9	99.9
	180 (open)		100	
	250 (open)			100.5
10.6	20	78.9	77.6	76.3
	40	95.9	96.2	95.9
	60	98.1	98.7	98.5
	250 (open)			100

**Table 3.2:** Data for 18 and 25 cm snouts, compared to 12 cm snout. Output in percent, relative to the values measured with a 120 mm diameter aperture and the 12 cm snout. The modulation width was 2 cm. The values for 180 mm and 250 mm field diameter were acquired with no aperture in place.

range [cm]	option	2nd scatterer	RM track	$\Psi_{\varnothing 20/120}$ [%]
5.8	A1	8	3	98.7
5.9	A2	8	6	98.8
11.6	A4	8	7	94.0
11.7	A5	2	5	94.4
19.8	A6	2	7	82.2
19.9	A7	2	8	83.1

**Table 3.3:** Influence of the second scatterer and range modulator track on field size effect. Modulation width was 2 cm.

because the output for fields of 20 mm diameter is notably decreased for all measured ranges.

1. **Second scatterer.** An impact of the combination of second scatterer would mean option dependence of the field size effect. The output was measured for two ranges differing by 1 mm, one at the high end of an option, the other at the low end of the next higher option, for transitions between option A1(5.8 cm)/A2(5.9 cm), A4(11.6 cm)/A5(11.7 cm) and A6(19.8 cm)/A7(19.9 cm). Airgap and modulation were kept constant at 8 cm and 2 cm, respectively. The experiments did not find a significant dependence on the option in use. The values listed in Table 3.3 show a trend of an increase of  $\Delta(\Psi_{\varnothing 20/120})$  per mm range with option (column 6), but it remains smaller than 1 %.
2. **Distance of the point of interest to distal 90 %.** We positioned the detector at a constant depth of 10.6 cm, and varied range and modulation such that the detector was at the calibration depth for the respective SOBP (i.e. at the center of the high dose region). The airgap was constant at 8 cm. This effect amounts to  $\approx 0.4$  % per cm distance between POI and distal 90 %, adding up to  $\approx 3$  % difference in between the minimum and maximum modulation measured (2 and 18.8 cm, respectively, Table 3.4).
3. **Airgap.** For range and modulation of 19 cm and 2 cm, we varied the airgap between 8 cm and 20 cm. Per cm change in airgap we observed 0.6 % change in  $\Psi_{\varnothing 20/120}$  (Table 3.5). This amounts to a maximum difference of 6.6% when varying the airgap from 8 to 20 cm. This difference can be almost entirely attributed to  $\Psi_{\varnothing 20}$  (Table

range [cm]	mod [cm]	$\Psi_{\varnothing 20/120}$ [%]
11.6	2	94.0
13.1	5	95.0
14.1	7	95.7
15.1	9	96.3
16.1	11	96.6
18.1	15	96.6
20.0	18.8	96.9

**Table 3.4:** Influence of the distance of the point of interest to the distal 90% depth. Relative output Measured at 10.6 cm depth

airgap	$\Psi_{\varnothing 20/120}$	$\Psi_{\varnothing 20/120(8cm)}$ [%]
8	82.2	100
14	79.5	96.5
20	75.6	91.5

**Table 3.5:** Influence of the air gap on field size effect. Relative output measured for a range and modulation of 19.8 cm and 2 cm. The third column ( $\Psi_{\varnothing 20/120}$  relative to  $\Psi_{\varnothing 20/120}$  for 8 cm airgap) shows that the decrease in output is largely caused by a decrease in  $\Psi_{\varnothing 20/120}$ .

3.5, column 3). The reference output for the large aperture changes only by 0.8 % for the 12 cm change in airgap.

### 3.2.4 Discussion

Extensive measurements in all our beamlines showed that the relation of relative output and field size cannot be fully explained by charged particle disequilibrium. Additional measurements in our gantry beamline revealed a weak dependence of the field size effect on option ( $\leq 1\%$ , Table 3.3), a notable influence of position of the point of interest with respect to the distal 90 % ( $\leq 3\%$ , Table 3.4) and a strong correlation to the airgap ( $\leq 6.6\%$ , see Table 3.5).

### Slit scatter as possible explanation

Our results point toward a dose contribution from scattered particles at calibration depth. Since there is no effect of snout size the snout walls can be excluded as possible source. The observed very small option-dependence may well be within the measurement uncertainty, ruling out an influence of the second scatterer and range modulator track. After eliminating those possibilities, the most likely source of a measurable scattered dose is the final collimator. This hypothesis is supported by the strong correlation of field size effect and modulation width as well as airgap. If the inner edge of the collimator acts as proton source, airgap dependence is explained to first order as inverse-square-effect, and modulation dependence arises from the increased number of protons needed to deliver the same dose at point of interest. The importance of collimator scatter was also pointed out by Titt *et al* [85], based on Monte Carlo simulations. Van Luijk *et al* [86] and Gottschalk [87] have previously described Monte Carlo simulations of collimator-scattered particles. Kimstrand *et al* [88] presented a parameterization of collimator scatter for accurate and fast dose calculation. Sahoo *et al* [89] presented a method for monitor unit calculation in passively scattered proton beams, incorporating a correction factor for the field size. The latter is, however, measured on a field-by-field basis for apertures smaller than 5x5 cm, and ignored for fields larger than that. We do not consider routine measurement of field size factors desirable since the data are extremely sensitive to setup uncertainties. The setup therefore has to be done very carefully and is very time consuming. Furthermore, depending on range and modulation, even fields larger than 5x5 cm can show 2% reduction in output. For high-accuracy monitor unit calculations it is necessary to account for the field size effect even for large fields. Recently, our experimental results were confirmed by Monte Carlo simulations [90].

### Clinical Implementation

In our clinical practice field size specific correction factors to the modeled output factors are applied to STAR and gantry treatment fields. Since the attempt to parameterize the data did not yield accurate enough results, this correction factor is derived by interpolation of the obtained data. As parameters for the interpolation we use the depth of the calibration point (center of the SOBP) and the equivalent diameter of the treatment field (calculated as the diameter of a circle with the same area as the actual field).

This is only an approximation, since the exact field shape is not taken into account. There might, however, be an appreciable influence of the field shape for larger and more irregular treatment volumes. This should be investigated further.

The method furthermore does not consider the influence of the position of the point of interest with respect to the distal 90%. In other words, our correction is based entirely on the depth of the calibration point, not considering the exact range and modulation of the field. This is justified by the data presented in section 3.2.3, which showed that the output of a 20 mm field relative to a 120 mm field changed by only  $\leq 3\%$  when varying the modulation by 16.8 cm. This change in the relative output with modulation width will be smaller for larger field sizes. The effect of neglecting a field's range and modulation – using the depth of the calibration point as parameter to derive the field size correction – will be small considering that fields that require large modulations require large apertures as well. To illustrate this we now look at the data for a 20 mm aperture where we would like to derive the field size correction factor to the output for a range of 13.1 cm and a modulation of 5 cm, reference depth 10.6 cm. In our clinical practice we would now interpolate between the data presented in Figure 3.15, and as a result use the factor 94.4%. The exact measurement gives 95.0%, a difference of 0.6%. For small fields the high dose region becomes increasingly skewed. We therefore use the POI rather than the range as parameter for the interpolation

The impact of the airgap is neglected in our procedure. The measurements presented in Figures 3.14 – 3.16 were obtained with an airgap of 8 cm (including the thickness of the range compensator), corresponding to the average clinical value.

Data depicted in Figure 3.5 show good agreement between measurements obtained under the same conditions with brass apertures and the mini-multileaf collimator. The airgap for both collimator types, however, will differ since the bulky MLC cannot be positioned as close to the patient as the smaller brass apertures. For optimum accuracy in MLC based IMPT delivery a separate data set should be gathered with this device for clinically relevant airgaps.

### 3.2.5 Conclusion

The field size dependence of the output factor cannot be fully explained by loss of fluence resulting from charged particle disequilibrium. Our data show a further change in output even for fields large enough for lateral equilibrium. This makes the impact of field size on

the output a significant factor for precise prediction models even for large treatment fields. Based on our results it is necessary to incorporate a field specific size correction factor into the output prediction models of two of our three differently designed beamlines, not only for small fields. In MLC based IMPT, the monitor unit calculation has to be corrected for the field size effect on a segment-by-segment basis.

# Chapter 4

## Conclusions

### 4.1 Summary of Results

The proton therapy field is rapidly shifting towards pencil beam scanning proton therapy. Passive scattering beamlines will, however, be part of the proton therapy landscape in the near and intermediate future as they were designed to be in service for multiple decades and as, more importantly, they can already provide the highest quality treatment for most of the patients that are currently being treated with proton therapy. The goal of our work was to investigate the details of using a multi-leaf collimator in such a passive-scattered proton beamline. In the introduction of this thesis we formulated four questions related to the use of an MLC in proton therapy. In this section we provide a brief summary of how we believe to have answered these questions.

#### **Can IMPT in fixed beamlines offer advantages with respect to conformal (passively scattered) proton therapy?**

The benefit of IMPT in an existing fixed horizontal passive scattering beamline is the widened range of applications for fixed proton beams with this technique. Dose distributions achievable for intra-cranial target locations with beam directions constrained to the coronal plane were qualitatively equal to plans calculated without restriction on beam angles. In some situations, however, dose to healthy brain may be increased. Chapter 2.1.

#### **Is it feasible to deliver IMPT with an MLC, considering treatment time and neutron dose?**

The technical feasibility of MLC based IMPT was examined and neutron dose estimated. We concluded that IMPT dose distributions can be sequenced into a reasonable number of segments that technically enables MLC based IMPT. Neutron dose is increased but is limited to an acceptable level with an optimized beamline design. Chapter 2.2.

### **What are the properties of a multileaf collimator in a proton beam?**

The quality of proton dose distributions shaped by multileaf collimators differs from the commonly applied custom milled apertures. Properties of one specific MLC optimized for photon therapy were measured and compared to custom brass apertures. Penumbrae were found to be slightly increased due to a combination of the effect of the ragged aperture outline, and the increased air gap. The influence of the airgap is beamline specific since it depends strongly on source-to-axis distance. Chapter 3.1. Further improvement may be achievable with a proton therapy – optimized MLC.

### **What is the relationship between peak dose and MLC field size?**

The correlation between proton output factor and field size was described in preparation of the IMPT delivery. A large data set was gathered to supply the accuracy needed for the delivery of many small fields that together will determine the 3D intensity and dose distribution. Chapter 3.2.

## **4.2 Limitations of this work**

Our segmentation study (Chapter 2.2) indicates that an IMPT intensity-distribution can be broken down into a deliverable number of intensity-segments. Our analysis does not address how to reproduce these intensity-segments by means of MLC leaf settings. Using the current setup for treatment planning and segmentation those leaf shapes would have to be set such that they produce a dose distribution similar enough to the one created with a scanned beam for the segmented intensity maps.

Dosimetric properties were investigated for just a single multileaf collimator, having a small leaf width. The mini-multileaf collimator used was originally designed to be used for stereotactic photon radiotherapy. We expect that MLCs that will be applied in clinical routine in proton therapy will have different design properties. For example, the effect of the jagged field outline on penumbra and conformality will be worse for wider leaves. Activation of the MLC device due to quasi-continuous exposure as part of

routine clinical operation may be a larger issue for larger devices. It should be stressed that although our results are specific to the device investigated, the methodology and the set of tests described remain valid.

In MLC based IMPT many segments delivered will be off-axis, while the data we presented in Chapter 3.2 was limited to field shapes that contain the central axis. Use of off-axis segments has consequences for the dose distributions. The main consequence is an increased penumbra on the medial side of the segment as, for example, indicated by Slopsema *et al* [91]. This effect should be measured and depending on its magnitude it will have to be included in the dose calculation. The magnitude of the effect depends on beamline source-to-axis distance, airgap, collimator thickness and distance to the field edge from the central axis.

Our studies were part of a project of extending the capabilities of our own fixed horizontal beam line. This beam line and its patient positioner have been specifically designed to treat intra-cranial tumors. The methodologies and results presented regarding neutron dose in Chapter 2.2.3 and Chapter 3.1.3, are also of value for the use of MLCs in the treatment of other tumor sites such as those located in the thorax and abdomen region. Regarding our segmentation study (Chapter 2.2), however, we believe it not to be directly applicable for such targets as they tend to have a much larger volume. They may therefore require many more segments than needed for the accurate treatment of smaller intra-cranial tumors, unless special measures are taken. Based on our segmentation study alone it can not be concluded that MLC-based IMPT is feasible for any tumor location.

### 4.3 Discussion

Multileaf collimators offer a range of applications to proton therapy. The most basic form of utilization is in 3D conformal proton therapy. This eliminates the need for custom milled apertures. It thereby reduces the cost of material and labor to fabricate these apertures and, more importantly, it simplifies treatment planning and treatment logistics. The implementation of a layer stacking method with leaf shape variable between range layers constitutes a more complex use of an MLC and can provide increased proximal conformality of proton dose distributions. The most complex method of dose delivery with an MLC is intensity modulated proton therapy.

One of the research topics in photon radiotherapy for the past few years has been direct aperture optimization (DAO, e.g. [92] and [93]). The benefits of DAO are that allows the user to directly control of the number of segments in a treatment, and that the optimized dose distribution is an accurate representation of what will be delivered. Without DAO the leaf-sequencing step that is necessary to translate an optimized intensity distribution into deliverable segments typically will lead to a degradation of the optimized dose distribution. Both these benefits of DAO are very valuable also for the clinical implementation of MLC-based IMPT. With optimization software based on DAO, the number of segments, and therefore the neutron dose to the patient, can be directly controlled. Ideally, an optimizer for MLC-based IMPT would, or could, also take into account the possibility of using small SOBPs rather than single pristine peaks for optimization (see Chapter 2.2).

In recent years emphasis in radiotherapy development has been placed on the application of adaptive radiotherapy. Proton therapy with custom made hardware makes adaptation of the treatment a logistical challenge and is currently applied in only very limited form and for few patients. Multileaf collimators add flexibility and open new possibilities to proton therapy in this regard.

Moving targets remain a major challenge for radiotherapy in general, and even more so for proton therapy. Multiple proton therapy institutes are working on strategies to safely treat moving targets with scanned proton beams. Fast rescanning of the target volume (e.g. [94] [95]), gating (e.g. [95] [96] [97]) and tracking (e.g. for photon therapy [98], and for particles [95] [99] [100]) are some of the strategies under development. If moving targets are to be treated with MLC based IMPT these strategies will have to be adapted to be feasible for MLC delivery. MLC based IMPT for moving targets will likely be too slow to allow multiple deliveries a practical way to reduce the effects of interplay similar to rescanning with pencil beam delivery. Depending on the time needed to deliver the treatment, gating may be too large a burden for the patient. Although beams eye view tumor tracking will be possible with an MLC, a major open question is how to address motion-induced density variations. Although it is possible to vary the energy for a proton-segment, the required energy variation may be different for various regions of the segment. Perhaps the treatment of moving tumors with MLC-based IMPT should be limited to those patients having only restricted target motion, and delivery techniques that inhibit or minimize target motion, such as breath-hold.

## 4.4 Future Directions

The multileaf collimator studied here was originally designed for photon therapy. The design can be optimized for proton therapy, with for example thinner leaves, straight edges or a material minimizing neutron production. The latter is not trivial considering mechanics of leaves moving closely next to each other.

Currently, using the MLC entails manually mounting it to the treatment head. Leaf shapes have to be manually loaded and set one by one. For applications in treatments the device has to be fully integrated into the treatment control system. This includes the pure mechanics, such as designing a hoisting mechanism. It includes software and electronics to automatically load and set leaf shapes. And it includes various interlocks to provide the necessary, redundant, safety features.

The treatment planning system has to accommodate dose calculation for collimation with an MLC. A commissioning procedure for the TPS has to be designed and executed. A mechanism has to be invented to produce data files that define a sequence of leaf shapes and proton energies for the treatment control system; as well as a redundant checking system on the integrity and validity of these files.

For quality assurance of MLC based IMPT dose distributions patient specific three-dimensional dosimetry is necessary. Unlike for IMRT there are no commercial solutions on the market as of yet. Currently, facilities employ ion chamber arrays to measure two-dimensional profiles at different depths. The design and implementation of a QA program will require additional resources.

## 4.5 Conclusion

Our work addressed a number of questions regarding the use of MLCs in passive-scattered proton beamlines. Dosimetric characteristics have been shown to be clinically acceptable and can be further improved by the design of a dedicated proton MLC. Although MLCs in proton therapy will not allow the same flexibility as pencil beam scanning, their use increases workflow efficiency and will enhance the capabilities of existing and future passive-scattered proton beamlines.







# Declaration

Hiermit versichere ich, dass ich die vorliegende Arbeit ohne unzulässige Hilfe Dritter und ohne Benutzung anderer als der angegebenen Hilfsmittel angefertigt habe; die aus fremden Quellen direkt oder indirekt übernommenen Gedanken sind als solche kenntlich gemacht. Die Arbeit wurde bisher weder in Inland noch im Ausland in gleicher oder ähnlicher Form einer anderen Prüfungsbehörde vorgelegt.



# Acknowledgements

There are so many people I owe most sincere thanks, it is very difficult to find the proper beginning.

I would like to thank Uwe Oelfke for giving me the opportunity to do a dissertation in his group. Great many thanks to Harald Paganetti and Alex Trofimov for the very productive and friendly collaboration. They have always given most helpful advice at the right time.

Through my profession as clinical medical physicist my PhD experience was certainly different from many others. Over time, learning more and more about real life in an oncology profession, priorities and point of view shift, and that also finds a reflection in scientific work. In that spirit I would like to thank my clinical colleagues at MGH.

Drs Helen Shih, Paul Chapman and Jay Loeffler have helped me gain an understanding of the bigger picture in radiation oncology by patiently explaining medical issues on countless occasions. I especially extend thanks to Helen for the wonderful collaboration on the work presented in chapter 2.1 of this thesis – and to her family for sparing her even during maternity leave.

I have learned much about treatment workflow from the radiation therapists at the proton center. My deepest gratitude to Missy Johnson and Tricia Donnellan for many much appreciated lessons.

Many thanks to the entire clinical physics group. Thank you to Hanne Kooy for giving me the opportunity to come to MGH; I have certainly never forgotten this. Many experiments for chapter 3.1 were done in long but fun late night hours together with Mark Bangert as part of his work as Diploma student. Thanks also to Renata Chmielewska for the collaboration on chapter 2.1.

I am particularly grateful to Elizabeth Dennis and Brian Winey. We have worked together for only short time, but all the more intensively and I was able to benefit greatly from your knowledge and personalities.

Last, but most importantly, Marc Bussière. I am writing this after six weeks in Switzerland. Having worked together for six years, it will take a while until I am used to not being able to just turn around and ask for your opinion. I keep a PostIt the drawer of my desk with your cell and home number. It's a pink PostIt in Liz's handwriting (I saved it when she left) that has been my phone-a-friend lifeline in the last years. A million thanks for your work ethics, your clinical physics insights and personal support!

Just recently I realized that usually for the first let's say 20 life years of a child a parent cannot expect true gratitude. Most of all not for the lost nerves and worries. Looking back I am most impressed with and thankful for my parent's ability to always support my decisions, although many of them must have been worrisome. Together with my brother, who has always been the most honest critic, and all my grandparents I have the most supportive family one could wish for.

To Antje - our friendship is growing into a series of wondrous events. I am most grateful for your presence over the last years, and for having you close once more. Curious what will come next!

To Anne - despite of the distance we have had over the past 10 years we never grew apart. I truly value your perspective on things - you always get me to see things in a different and unexpected light. Your balance helped me much in the past eventful years.

Martijn! You are mingling in every aspect of my life – the private, the clinical and the PhD work. No doubt you will be as relieved as I once the latter is finished. Fifty-five huge thanks for always rallying for my sanity, and never imposing an SEP-field on my issues. Thank you!





# Bibliography

- [1] J Daartz, M Engelsman, H Paganetti, and M Bussi ere. Field size dependence of the output factor in passively scattered proton therapy: influence of range, modulation, air gap, and machine settings. *Med. Phys.*, 36:3205–10, 2009.
- [2] J Daartz, M Bangert, M Bussi ere, M Engelsman, and H Kooy. Characterization of a mini-multileaf collimator in a proton beamline. *Med. Phys.*, 36:1886–94, 2009.
- [3] J Daartz. Dosimetry of small fields in proton radiotherapy – verification of the cms focus dose computation software. *Diplomarbeit*, 2005.
- [4] J Daartz, M Bangert, M Bussi ere, M Engelsman, and H Kooy. Characterization of an mmlc in a proton beam. *AAPM*, 2008.
- [5] J Daartz, M Engelsman, and M Bussi ere. Field size dependence of the output factor in proton radiotherapy. *PTCOG*, 2008.
- [6] J Daartz, M Bangert, M Bussi ere, M Engelsman, and H Kooy. Acceptance testing of a commercial mini-multileaf collimator in a proton radiotherapy beamline. *PTCOG*, 2008.
- [7] J Daartz, A Trofimov, and H Paganetti. Feasibility study of mlc based impt. *PTCOG*, 2009.
- [8] International Commission on Radiation Units and Measurements (ICRU). *International Commission on Radiation Units and Measurements Dose specification for reporting external beam therapy with photons and electrons*. ICRU, 1978.
- [9] International Commission on Radiation Units and Measurements (ICRU). *Prescribing, recording, and reporting photon beam therapy (Supplement to ICRU Report 50)*. ICRU, 1999.
- [10] S Webb. The physical basis of imrt and inverse planning. *Br. J. Radiol.*, 76:678–89, 2003.

- 
- [11] T Bortfeld. Imrt: a review and preview. *Phys Med Biol.*, 51(13):R363–79, 2008.
- [12] S Webb. *The Physics of Conformal Radiotherapy: Advances in Technology*. Institute of Physics Publishing, 1997.
- [13] C Thieke, K H Kuefer, M Monz, A Scherrer, F Alonso, U Oelfke, P E Huber, J Debus, and T Bortfeld. A new concept for interactive radiotherapy planning with multicriteria optimization: first clinical evaluation. *Radiother Oncol*, 85:292–8, 2007.
- [14] D Craft and M Monz. Simultaneous navigation of multiple pareto surfaces, with an application to multicriteria imrt planning with multiple beam angle configurations. *Med Phys*, 37:292–8, 2010.
- [15] D Shepard, M Earl, X Li, S Naqvi, and C Yu. Direct aperture optimization: a turnkey solution for step-and-shoot imrt. *Med. Phys.*, 29:1007–18, 2002.
- [16] J Bedford. Treatment planning for volumetric modulated arc therapy. *Med Phys*, 36:4309–19, 2009.
- [17] C Men, X Jia, and SB Jiang. Gpu-based ultra-fast direct aperture optimization for online adaptive radiation therapy. *Phys. Med. Biol.*, 55:4309–19, 2010.
- [18] F Khan. *The Physics of Radiation Therapy*. Lippincott Williams & Wilkins, fourth edition, 2009.
- [19] H Bethe. Zur theorie des durchgangs schneller korpuskularstrahlen durch materie. *Annalen der Physik*, 397:325–400, 1930.
- [20] E Berger. Stopping powers and ranges for protons and alpha particles. *ICRU Report 49*, 1993.
- [21] J Janni. Proton range-energy tables, 1kev - 10 gev. *Atomic Data and Nuclear Data Tables 27 parts 1 (compounds) and 2 (elements)*, (Academic Press, 1982), 1982.
- [22] H Eidelman. Review of particle physics. *Phys. Lett.*, page B592, 2004.
- [23] Particle Data Group. <http://pdg.lbl.gov>.
- [24] G Molière. Theorie der streuung schneller geladener teilchen 1, einzelstreuung am abgeschirmten coulomb-feld. *Z. Naturforschg. 2a*, pages 133– 145, 1947.
- [25] G Moliere. Theorie der streuung schneller geladenen teilchen 2, mehrfach- und

- vielfachstreuung. *Z. Naturforschg. 3a*, pages 78–97, 1948.
- [26] V Highland. Some practical remarks on multiple scattering. *Nucl. Instr. Meth.*, 129:497–499, 1975.
- [27] V L Highland. Erratum: Some practical remarks on multiple scattering. *Nucl. Instr. Meth.*, 161:171, 1979.
- [28] S Safai, T Bortfeld, and M Engelsman. Comparison between the lateral penumbra of a collimated double-scattered beam and uncollimated scanning beam in proton radiotherapy. *Phys Med Biol.*, 53:1729–50, 2008.
- [29] A Holmes-Siedel and L Adams. *Handbook of Radiation Effects*. Oxford University Press, second edition, 2002.
- [30] M Engelsman, H Lu, D Herrup, M Bussière, and H Kooy. Commissioning a passive-scattering proton therapy nozzle for accurate sobp delivery. *Med Phys*, 63: 2172–80, 2009.
- [31] C Ainsley, Scheuermann, S Avery, D Dolney, R Maughan, and J McDonough. Monte carlo simulation and development of a multileaf collimator for proton therapy. *Annual AAPM Meeting*, 2009. Moderated Poster Presentation July 2009.
- [32] A Lomax. Intensity modulation methods for proton radiotherapy. *Phys. Med. Biol.*, 44:185205, 1999.
- [33] P Chapman, C Ogilvy, and W Butler. *A new stereotactic alignment system for charged particle radiosurgery at the Harvard Cyclotron Laboratory, Boston*, pages 105–108. New York: McGraw-Hill, 1992.
- [34] M Bussière and J Adams. Treatment planning for conformal proton radiation therapy. *Technol. Cancer Res. Treat.*, 2:389–99, 2003.
- [35] International Commission on Radiation Units, Measurements, and International Atomic Energy Agency. *Prescribing, recording and reporting proton-beam therapy*. Oxford University Press, 1999.
- [36] H Kooy, B Clasio, H Lu, T Madden, H Bentefour, N Depauw, J Adams, A Trofimov, D Demaret, T Delaney, and J Flanz. A case study in proton pencil-beam scanning delivery. *Int J Radiat Oncol Biol Phys*, 76:642–630, 2010.
- [37] W Chen, D Craft, T M Madden, K Zhang, H M Kooy, and G T Herman. A

- fast optimization algorithm for multicriteria intensity modulated proton therapy planning. *Med Phys*, 37:4938–45, 2010.
- [38] A Nimierko. A generalized concept of equivalent uniform dose. abstract. *Med Phys*, 26:1100, 1999.
- [39] D Baltas, C Kolotas, K Geramani, R F Mould, G Ioannidis, M Kekchidi, and N Zamboglou. A conformal index (coin) to evaluate implant quality and dose specification in brachytherapy. *Int J Radiat Oncol Biol Phys.*, 40:515–24, 1998.
- [40] G Sharp. <http://www.liu.edu/cwis/cwp/library/workshop/citama.htm>.
- [41] J Unkelbach, T Bortfeld, B C Martin, and M Soukup. Reducing the sensitivity of impt treatment plans to setup errors and range uncertainties via probabilistic treatment planning. *Med Phys*, 36:149–63, 2009.
- [42] S M Macdonald, A Trofimov, S Safai, J Adams, B Fullerton, D Ebb, N J Tarbell, and T I Yock. Proton radiotherapy for pediatric central nervous system germ cell tumors: Early clinical outcomes. *Int J Radiat Oncol Biol Phys*, 2010. epub ahead of print.
- [43] M Steneker, A Lomax, and U Schneider. Intensity modulated photon and proton therapy for the treatment of head and neck tumors. *Radiother Oncol*, 80:263–7, 2006.
- [44] S MacDonald, S Safai, A Trofimov, J Wolfgang, B Fullerton, B Yeap, T Bortfeld, N Tarbell, and T Yock. Proton radiotherapy for childhood ependymoma: initial clinical outcomes and dose comparisons. *Int J Radiat Oncol Biol Phys*, 71:979–86, 2008.
- [45] L Cozzi, A Fogliata, A Lomax, and A Bolsi. A treatment planning comparison of 3d conformal therapy, intensity modulated photon therapy and proton therapy for treatment of advanced head and neck tumours. *Radiother Oncol*, 61:287–97, 2001.
- [46] A Bolsi, A Fogliata, and L Cozzi. Radiotherapy of small intracranial tumours with different advanced techniques using photon and proton beams: a treatment planning study. *Radiother Oncol*, 68:1–14, 2003.
- [47] B Baumert, I Norton, A Lomax, and J Davis. Dose conformation of intensity-modulated stereotactic photon beams, proton beams, and intensity-modulated proton beams for intracranial lesions. *Radiother Oncol*, 61:287–97, 2006.

- [48] Z Moravek, M Rickhey, M Hartmann, and L Bogner. Uncertainty reduction in intensity modulated proton therapy by inverse monte carlo treatment planning. *Phys. Med. Biol*, 54:4803–19, 2009.
- [49] M Bangert and U Oelfke. Robust spot placement for impt in combination with beam angle optimization. *Poster presentation PTCOG 49*, 2010.
- [50] E J Hall. The impact of protons on the incidence of second malignancies in radiotherapy. *Technol Cancer Res Treat*, 6:31–4, 2007.
- [51] H Paganetti. The impact of protons on the incidence of second malignancies in radiotherapy by eric j. hall supp.31-34 2007. *Technol Cancer Res Treat*, 6:661–2, 2007.
- [52] S Nill. Development and application of a multi-modality inverse treatment planning system. *PhD thesis*, 2001.
- [53] H Paganetti. Accurate monte carlo simulations for nozzle design, commissioning and quality assurance for a proton radiation therapy facility. *Med Phys*, 31:2107–18, 2004.
- [54] T Bortfeld, U Oelfke, and S Nill. What is the optimum leaf width of a multileaf collimator. *Med Phys*, 27:2494–2501, 2000.
- [55] K Engel. A new algorithm for optimal multileaf collimator field segmentation. *Discrete Applied Mathematics*, 152, 2005.
- [56] Bernhard Gottschalk. <http://huhepl.harvard.edu/~gottschalk>.
- [57] D Hecksel, V Anferov, M Fitzek, and K Shahnazi. Influence of beam efficiency through the patient-specific collimator on secondary neutron dose equivalent in double scattering and uniform scanning modes of proton therapy. *Phys. Med. Biol*, 37, 2010.
- [58] National Council on Radiation Protection & Measurements. Structural shielding design and evaluatopn for megavoltage x- and gamma-ray radiotheraoy facilities. 2005.
- [59] Basit Athar, Bryan Bednarz, Joao Seco, Cindy Hancox, and Harald Paganetti. Comparison of out-of-field photon doses in 6 mv imrt and neutron doses in proton therapy for adult and pediatric patients. *Phys. Med. Biol*, 55:2879–2891, 2010.

- [60] D Brenner, C Elliston, E Hall, and H Paganetti. Reduction of the secondary neutron dose in passively scattered proton radiotherapy, using an optimized pre-collimator/collimator. *Phys. Med. Biol.*, 54, 2009.
- [61] R J Schneider A M Koehler and J M Sisterson. Range modulators for protons and heavy ions. *Med. Phys.*, 131:437–40, 1975.
- [62] A M Koehler; R J Schneider; J M Sisterson. Flattening of proton dose distributions for large fields. *Nucl. Instrum. Methods*, 4:297–301, 1977.
- [63] M Torikoshi; S Minohara; N Kanematsu; M Komori; M Kanazawa; K Noda; N Miyahara; H Itoh; M Endo; T Kanai. Irradiation system for himac. *J Radiat Res (Tokyo)*., 48:A15–25, 2007.
- [64] N Kanematsu; M Endo; Y Futami; T Kanai; H Asakura; H Oka; K Yusa. Treatment planning for the layer-stacking irradiation system for three-dimensional conformal heavy-ion radiotherapy. *Med Phys.*, 29:2823–9, 2002.
- [65] T Kanai; N Kanematsu; S Minohara; M Komori; M Torikoshi; H Asakura; N Ikeda; T Uno; Y Takei. Commissioning of a conformal irradiation system for heavy-ion radiotherapy using a layer-stacking method. *Med Phys.*, 33:2989–97, 2006.
- [66] M Torikoshi; S Minohara; N Kanematsu; M Komori; M Kanazawa; K Noda; N Miyahara; H Itoh; M Endo; T Kanai. Irradiation system for himac. *J Radiat Res (Tokyo)*., 48:A15–25, 2007.
- [67] A N Schreuder. A small ionisation chamber for dose distribution measurements in a clinical proton beam. *Advances in Hadrontherapy*, pages 284–289, 1997.
- [68] M Bangert. Dosimetric properties of a proton multileaf collimator simulation and experimental validation. *Diplomarbeit*, 2007.
- [69] Mutic S Low D A, Harms W B and Purdy; J A. A technique for the quantitative evaluation of dose distributions. *Medical Physics*, 25:656–661, 1997.
- [70] P J Binns and J H Hough. Secondary dose exposures during 200mev proton therapy. *Radiat. Prot. Dosim.*, 70:441–444, 1997.
- [71] S Agosteo. Secondary neutron and photon dose in proton therapy. *Radiother. Oncol.*, 48:293–305, 1998.
- [72] U Schneider. Secondary neutron dose during proton therapy using spot scanning.

- Int. J. Radiat. Oncol., Biol., Phys*, 53:244–251, 2002.
- [73] X Yan; U Titt; A M Koehler and W D Newhauser. Measurement of neutron dose equivalent to proton therapy patients outside of the proton radiation field. *Nucl. Instrum. Methods Phys. Res A*, 476:429–434, 2002.
- [74] S C Roy and G A Sandison. Scattered neutron dose equivalent to a fetus from proton therapy of the mother. *Radiat. Phys. Chem.*, 71:997–998, 2004.
- [75] H Jiang *et. al.* Simulation of organ-specific patient effective dose due to secondary neutrons in proton radiation treatment. *Phys. Med. Biol.*, 50:4337–4353, 2005.
- [76] J C Wolf and W D Newhauser. Calculation of neutron dose equivalent exposures from range-modulated proton therapy beams. *Phys. Med. Biol.*, 50:3859–3873, 2005.
- [77] Mesoloras. Neutron scattered dose to fetus from proton radiotherapy. *Med. Phys.*, 33:2479–2490, 2006.
- [78] Wroe; Rosenfeld and Schulte. Out-of-field dose equivalents delivered by proton therapy of prostate cancer. *Med. Phys.*, 34:3449–3456, 2007.
- [79] V Anferov. Analytic estimates of secondary neutron dose in proton therapy. *Phys Med Biol*, 55, 2010.
- [80] E W Cascio, J M Sisterson, and R Slopsema. Secondary neutron fluence in radiation test beams at the northeast proton therapy center. *Workshop, 2005. IEEE*, pages 175–78, 2005.
- [81] A Wroe, B Clasie, H Kooy, J Flanz, R Schulte, and A Rosenfeld. Out-of-field dose equivalents delivered by passively scattered therapeutic proton beams for clinically relevant field configurations. *Int J Radiat Oncol Biol Phys*, 73:306–13, 2009.
- [82] H M Kooy, S J Rosenthal, M Engelsman, A Mazal, R L Slopsema, H Paganetti, and J B Flanz. Commissioning a passive-scattering proton therapy nozzle for accurate sobp delivery. *Phys Med Biol*, 50:847–856, 2005.
- [83] J D Fontenot, W D Newhauser, C Bloch, R A White, U Titt, and G Starkschall. Determination of output factors for small proton therapy fields. *Med Phys*, 34: 489–98, 2007.
- [84] L Hong. A pencil beam algorithm for proton dose calculations. *Phys. Med. Biol.*,

- 41:1305–1330, 1996.
- [85] Titt U; Zheng Y; Vassiliev ON and Newhauser WD. Monte carlo investigation of collimator scatter of proton-therapy beams produced using the passive scattering method. *Phys Med Biol.*, 53:487–504, 2008.
- [86] van Luijk P; van t' Veld AA; Zelle HD; Schippers JM. Collimator scatter and 2d dosimetry in small proton beams. *Phys Med Biol.*, 46:653–70, 2001.
- [87] B Gottschalk. Slit scattering. *unpublished*, 2007.
- [88] Kimstrand P; Traneus E; Ahnesj A; Tilly N. Parametrization and application of scatter kernels for modelling scanned proton beam collimator scatter dose. *Phys Med Biol.*, 53:3405–29, 2008.
- [89] N Sahoo, X Zhu, G Arjomandy, G Ciangaru, M Lij, R Amos, R Wu, and M Gillin. A procedure for calculation of monitor units for passively scattered proton radiotherapy beams. *Med. Phys.*, 35:5088–97, 2008.
- [90] B Bednarz, J Daartz, and H Paganetti. Dosimetric accuracy of planning and delivering small proton therapy fields. *Phys Med Biol.*, 55:7425–38, 2010.
- [91] R Slopsema and H Kooy. Incorporation of the aperture thickness in proton pencil-beam dose calculations. *Phys. Med. Biol.*, 51, 2006.
- [92] M Broderick, M Leech, and M Coffey. perture optimization as a means of reducing the complexity of intensity modulated radiation therapy plans. *Radiat Oncol*, 16:4:8, 2009.
- [93] C Yu, D Shepard, M Earl, D Cao, S Luan, C Wang, and D Chen. New developments in intensity modulated radiation therapy. *Technol Cancer Res Treat*, 5, 2006.
- [94] S Zenklusen, E Pedroni, and D Meer. A study on repainting strategies for treating moderately moving targets with proton pencil beam scanning at the new gantry 2 at psi. *Phys. Med. Biol*, 55, 2010.
- [95] E Rietzel and C Bert. Respiratory motion management in particle therapy. *Med. Phys.*, 37, 2010.
- [96] H Lu, R Brett, G Sharp, S Safai, S Jiang, and J Flanz. A respiratory-gated treatment system for proton therapy. *Med. Phys.*, 34, 2007.
- [97] S Minohara, T Kanai, M Endo, K Noda, and M Kanazawa. Respiratory gated

- irradiation system for heavy-ion radiotherapy. *Int J Radiat Oncol Biol Phys*, 47, 2000.
- [98] P Keall, V Kini, S Vedam, and R Mohan. Motion adaptive x-ray therapy: a feasibility study. *Phys Med Biol*, 46, 2001.
- [99] S Grzinger, C Bert, T Haberer, G Kraft, and E Rietzel. Motion compensation with a scanned ion beam: a technical feasibility study. *Radiat Oncol*, 14:3:34, 2008.
- [100] S vandeWater, R Kreuger, S Zenklusen, E Hug, and A Lomax. Tumour tracking with scanned proton beams: assessing the accuracy and practicalities. *Phys Med Biol*, 54, 2009.